LABORATORY MEASUREMENTS OF ELECTRICAL RESISTIVITY OF KEROGEN IN ORGANIC-RICH MUDROCKS

A Thesis

by

GAMA ADAM FIRDAUS

Submitted to the Office of Graduate and Professional Studies of
Texas A&M University
in partial fulfillment of the requirements for the degree of

MASTER OF SCIENCE

Chair of Committee,	Zoya Heidari
Committee Members,	Walter B. Ayers
	Andreas Kronenberg
Head of Department,	Daniel Hill

August 2015

Major Subject: Petroleum Engineering

Copyright 2015 Gama Adam Firdaus

ABSTRACT

Reliability of conventional resistivity-porosity-saturation models (e.g., dual water and Waxman-Smits) is questionable in organic-rich mudrocks, which often leads to overestimation of water saturation. Previous publications showed that the interpretation of electrical resistivity logs for such rocks is challenging because of the presence of highly mature kerogen and pyrite connected networks that can influence electrical resistivity measurements. However, the electrical properties of kerogen in these rocks have not yet been quantified experimentally. Separation of kerogen from mudrocks and subsequent removal of pyrite from the kerogen, both requirements for successful laboratory experiments, remain challenging. This research quantitatively evaluated the electrical resistivity of mature kerogen using an experimental approach.

This thesis was designed to assess the impact of maturity on electrical resistivity of the isolated kerogen and organic-rich mudrock samples at heat-treated samples ranging from 25°C to 800°C. Kerogen isolation was performed on mudrock samples, using a physical method, chemical techniques, and pyrite removal that involved acidic chromium chloride solution under a nitrogen (N_2) atmosphere. The isolated kerogen powder sample was then compressed to form a homogeneous consolidated disk using a mold frame designed for this purpose. The next step was to synthetically mature both mudrock and isolated kerogen samples by heat-treating. Finally, the last step of the experimental work is to measure the electrical resistivity and geochemical properties of each set of molded samples at different

maturity levels. The actual electrical resistivity of kerogen was estimated by minimizing the difference between the numerically simulated and measured effective electrical resistivity of the molded kerogen samples.

The experimental work successfully isolated kerogen from Haynesville mudrock samples. X-ray fluorescence (XRF) measurements confirmed the absence of carbonates, silicates, and pyrite in the isolated kerogen samples. The electrical resistivity measurements of these samples recorded a significant decrease (i.e., up to four orders of magnitude) upon elevating the heat-treatment temperature from 300°C to 800°C. The decrease of electrical resistivity at high maturity levels could be attributed to the presence graphite-like sheets and/or the appearance of aromatic components in the organic matter. Further investigation is required to accurately separate the impact of different factors affecting electrical resistivity in the isolated kerogen and organic-rich mudrock samples. The outcomes of this thesis can potentially improve interpretation of electrical resistivity logs in organic-rich mudrocks, which can lead to enhanced well-log-based assessment of in situ hydrocarbon saturation.

DEDICATION

This thesis is dedicated to my creator, ALLAH SWT, to my lovely and amazing mother, father, sister, and to my home country, Indonesia.

ACKNOWLEDGEMENTS

In the name of ALLAH, the Beneficent, the Merciful.

I would like to express my gratitude to my creator, ALLAH SWT, for giving me strength, knowledge, and guidance to finish this master thesis. All praise is for Him, who gives mankind the knowledge they never had before.

I would like to thank my advisor, Dr. Zoya Heidari, for her guidance, constructive comments, valuable insights and analysis, remarks and engagement through the conduct of this thesis. I also appreciate the help and support from the members of my committee, Dr. Walter B. Ayers and Dr. Andreas Kronenberg for suggestions, guidance, assistance and patience from time to time during the process of this research. I would like to thank Dr. Thomas A. Blasingame for his attendance in my thesis defense as the substitute committee and his constructive comments on my thesis.

I thank all my colleagues in the Multi-Scale Formation Evaluation Research Group, especially, Huangye Chen, Emmanuel Oyewole, Abdelrahman Kotb, and Angie Yang for their help and support in the completion of this thesis. I appreciate all the companies and organizations that fund and support this research, such as: American Chemical Society, Crisman Institute for Petroleum Research, and SPE International and the Multi-Scale Formation Evaluation Joint Industry Project. Thanks also goes to the Harold Vance

Department of Petroleum Engineering staff and administration for being extremely helpful during my time in the department. I would like to thank Dr. Mike Tice, who trained me to use the XRF equipment and shared the knowledge to analyze the results. I appreciate Texas A&M Supercomputing Facility for providing computing resources used for the numerical simulations in this thesis.

I further extend my appreciation to my best friends and roommates, Danar Sampurno and Farid Bakti, for all of their encouragement and help in cheerful and difficult times. They have been always there for me, and so will I. Thanks and gratitude are also given to all members of the Multi-Scale Formation Evaluation TAMU research group for sharing valuable knowledge, support, and cheers. I am indebted to Gia Alexander for the advice and constructive remarks through this thesis writing. Furthermore, I would like to express my big appreciation for John Maldonado and Don Conlee for supporting my experimental instruments and supervising the safety of the laboratory experiments.

Beyond Texas A&M University, I am grateful to the research scientists of W.D. Von Gonten Laboratories, Devon McAfee, Eric Carter, Debora Berti, Scott Davis, Andrew Russell, and Michael Stewart for sharing technical assistance on experimental procedures and results with me.

Last but not least, my sincere thanks and gratitude is to my mom, dad, and sister for warm love, endless support, and help throughout the entire process, both keeping me focus and helping me putting pieces together to finish this thesis.

NOMENCLATURE

List of Acronyms

2D	Two-Dimensional
3D	Three-Dimensional
Al	Aluminum
Ca^{2+}	Calcium
$CaCl_2$	Calcium Chloride
$CaCO_3$	Calcium Carbonate
CaF_2	Calcium Fluoride
$CrCl_2$	Chromium Chloride
CO_2	Carbon Dioxide
CO	Carbon Monoxide
Cl^-	Chloride
CT	Computed Tomography
DC	Direct Current
DCM	Dichloro Methane
EDXRF	Energy Dispersive X-Ray Fluorescence
F^-	Fluoride
Fe	Iron
$FeCl_2$	Iron Chloride

FeS_2	Pyrite
FID	Flame Ionization Detector
HCl	Hydrochloric acid
HF	Hydroflouric acid
HI	Hydrogen Index, mg HC/g TOC
HNO_3	Nitric Acid
H_2S	Sulfuric Acid
K	Potassium
LAH	Lithium Aluminum Hydride
Mn	Manganese
NaOH	Sodium Hydroxide
OI	Oxygen Index, mg CO_2/g TOC
S	Sulfur
Si	Silica
TEM	Transmission Electron Microscope
Ti	Titanium
TiO_2	Titanium Oxide
TOC	Total Organic Carbon, wt%
XRD	X-Ray Diffraction
XRF	X-Ray Flouresence
Zn	Zinc

List of Symbols

A	Cross-Sectional Area, cm^2
D	Diameter, cm
I	Electric Current, A
h	Thickness, cm
M	Molarity
N	Normality
R	Electrical Resistance, ohm
V	Electric Potential, V
ΔV	Electric Potential Difference, V
v/v	Volume/Volume
v/w	Volume/Weight
W	Watt
ρ	Electrical Resistivity, ohm-m
σ	Electrical Conductivity, S/m

TABLE OF CONTENTS

Page

LIST OF FIGURES

Page

LIST OF TABLES

Page

CHAPTER I

INTRODUCTION AND LITERATURE REVIEW

The impacts of kerogen's maturity on electrical resistivity of organic-rich mudrocks are essential to improve the assessment of hydrocarbon saturation. Using laboratory experiments, this research quantitatively evaluated the electrical resistivity of kerogen at different maturity levels. This chapter elaborates the background of this topic and presents its outline, statement of the problem, and research objectives.

1.1 Background

This background section is organized into three main parts. The first part addresses the challenge of petrophysical evaluation in organic-rich mudrocks. The next subsection explains precedent studies regarding experimental techniques of isolating kerogen from organic-rich mudrocks. The final subsection shows previous research that investigates the impact of kerogen maturity on electrical resistivity of organic-rich mudrocks. This subsection presents a comprehensive literature review to establish the current status of the questions this thesis research explored.

1.1.1 The Challenge of Petrophysical Evaluation in Organic-rich Mudrocks

There are several causes of difficulties in the evaluation of petrophysical properties of organic-rich mudrocks. These include complex pore types and distribution (Milner et al.

2010; Passey et al. 2010; Sondergeld et al. 2010; Curtis et al. 2011; Sondergeld et al. 2013; Saidian et al. 2014), geometries of connected and disconnected pores that reside in the organic matter and inorganic matrices. (Sisk et al. 2010; Curtis et al. 2012; Sondergeld et al. 2013; Wang et al. 2014), and variation in electrical resistivity of formation water, mature kerogen, and conductive minerals such as pyrite (Passey et al. 2010; Clennell et al. 2010; Kethireddy et al. 2014).

The complex physical properties of organic-rich mudrocks are not taken into account in conventional well-log interpretation methods. For example, conventional well-log interpretation methods such as Archie's (Archie 1942), Dual-Water (Clavier et al. 1984), and Waxman-Smits (Waxman and Smits 1968) equation are commonly used to assess fluid saturations from electrical resistivity logs in organic-rich mudrocks. These models take electrical resistivity logs as input, which are influenced by the conductive materials in the rock. An obvious feature of these conventional models is that they consider the effective electrical resistivity of the rock to be influenced only by the presence of formation water in the rock. In organic-rich mudrocks, however, the presence of highly mature kerogen and pyrite can possibly impact electrical resistivity (Passey et al. 2010). Therefore, applying only the aforementioned models when interpreting petrophysical properties in organic-rich mudrocks causes uncertainties in the assessment of fluid saturations, which can ultimately impact the reserve estimation. However, no studies have yet quantified the electrical resistivity of kerogen isolated from organic-rich mudrocks at different maturity levels.

1.1.2 Kerogen Isolation

Kerogen is commonly defined as the insoluble organic matter that exists in organic-rich mudrocks (Durand 1980). Kerogen is a complex mixture of organic material, and its chemical composition differ within and between formations. Vandenbroucke and Largeau (2007) stated that kerogen is best characterized experimentally, based on its insolubility. However, this definition fails because the organic fraction may contain insoluble residues that cannot form oil or gas in the stage of maturation.

In general, the main objective of organic matter extraction is to separate the organics from the minerals for laboratory investigation of the organic matrix. Mechanisms of natural demineralization have been performed artificially in several research fields, such as geochemistry, paleontology, soil engineering, and petroleum engineering. Over recent decades, additional studies have applied specialized techniques to extract kerogen (organic matter) from organic-rich mudrocks.

The three main techniques of obtaining kerogen from organic-rich mudrocks are (a) physical methods, (b) thermal methods, and (c) chemical methods/demineralization.

1.1.2.1 Physical Methods

The most common physical methods to remove minerals from organic-rich mudrocks are grinding, gravity segregation, and centrifugation (Robinson 1969; Durand and Nicaise 1980). Quass (1939) physically recovered organic matter from the rock using differential wettability. In this method, the differential wettability between the kerogen which is oil

wet, and the mineral matrix which is water wet, separates the organic matter from other mineral components in the rock. Hubbard et al. (1952) used a centrifugation method to separate kerogen from finely ground organic-rich mudrock sample in a liquid media. The density of the liquid media is between that of the kerogen and minerals. Hubbard et al. (1952) reported that the centrifugation method was able to recover 2% of kerogen.

The physical methods are advantageous because they prevent alteration of the chemical structure of the kerogen (Forsman 1963; Saxby 1970; Vandenbroucke and Largeau 2007). However, physical methods are not effective techniques to remove the minerals from organic-rich mudrocks, as it is tedious, lengthy, and costly. Although there have been various degrees of success, in general, the physical method to isolate kerogen from other minerals has a low recovery rate (Smith 1961; Forsman 1963; Durand and Nicaise 1980). Furthermore, the result of performing this method does not represent an accurate chemical composition of the in situ kerogen. The recovery rate of kerogen via this method can be improved by successive crushing, repeated operations, and combined with chemical isolation methods.

1.1.2.2 Thermal Methods

In some studies, extracting kerogen is defined as taking only the organic matter from the organic-rich mudrocks by altering it into moveable hydrocarbon (Harwood 1977). This technique is the thermal method which uses heat to decompose kerogen. The two most common experimental techniques for the thermal method are in situ and ex situ retorting (Smith et al. 2007). The heating element is lowered into the well and heats the kerogen,

slowly converting it into oil and gas. However, the major drawback of this method is that the chemical structure of the organic matter changes. Therefore the application of this method is not suitable for this research.

1.1.2.3 Chemical Methods

Chemical methods are considered among the best for isolating kerogen from organic-rich mudrocks (Saxby 1970). The main procedures in the chemical isolation method are (a) bitumen removal, which extracts the moveable bitumen using solvent extraction method and (b) acid demineralization, which dissolves carbonates, silicates, feldspars, and clays.

Tamimi and Uysal (1990) explained that the bitumen extraction process involves a physicochemical interaction between the organic solvent and rock sample. In their study, a mixture of 75% benzene and 25% cyclohexane was used. In an ideal setting, the bitumen removal process would be performed in every stage of the kerogen isolation (i.e., before and after acid demineralization procedure). Durand and Nicaise (1980) suggested that this process should be performed before the acid treatment in order to prevent any chemical alterations of the soluble bitumen and possibly the kerogen. However, since solvent extraction only removes the moveable bitumen from the sample, such treatment does not alter the chemical integrity of the kerogen and affect the mineral fraction. Therefore, Vandenbroucke and Largeau (2007) performed bitumen removal before and after the demineralization of the rock sample. To maintain the chemical structure of the kerogen, Goklen et al. (1984) reported that using reactive solvents and performing the experiments under high temperatures should be avoided.

Solvents that have been used to extract the soluble bitumen from organic-rich mudrocks include benzene; a mixture of toluene, chloroform, and methanol; dichloromethane (DCM), hexane, ethanol, and chloroform. Lamey and Childers (1977) used benzene for each gram (10:1 v/w) of organic shale to be extracted. Goklen et al. (1984) suggested that bitumen removal should use a mixture of toluene and methanol with the ratio of 3:1. In 2011, Torrente and Galan (2011) compared the extraction ability of toluene to methanol and showed that the quantity of bitumen extracted increases as the amount of toluene in the mixtures increases.

Vandenbroucke (2003) suggested that DCM is preferred as a solvent, since it can efficiently extract the bitumen, which mainly consists of moveable hydrocarbon. However, DCM is costly compared to chloroform, which has a similar ability to extract the bitumen from organic-rich mudrock samples without altering the chemical integrity of the organic matter (Durand and Nicaise, 1980; Aboulkas and El-Harfi, 2009). Chloroform has been proved to obtain higher bitumen yields compared to ethanol, hexane, and toluene (Al-Harasheh, 2011).

McIver (1962) successfully performed the solvent extraction in combination with ultrasonic treatment for extracting soluble organic matter from sediments. McIver (1962) used the mixture of 70% benzene and 15% each of acetone and methanol as the organic solvents. In the same experiment, the ultrasonic treatment was done for only five minutes. McIver reported that the soluble organic matter regained from four different shale samples

was higher upon using the ultrasonic method than the Soxhlet extraction method. A similar method, which repeatedly used chloroform and ultrasonification, was also performed to extract the soluble organic matter from organic shale (Lis et al. 2008; Zhao et al. 2013). Zhao et al. (2013) showed that ultrasonic extraction using a mixture of 60:40 (wt%) of chloroform and carbon disulfide was able to extract moveable bitumen up to 15.6% of the sample that has been treated with acid.

In the case of acid demineralization, the most common acids used to isolate kerogen from organic-rich mudrocks are hydrochloric acid (HCl) and hydrofluoric acid (HF). The main objective of the HCl treatment is to remove most carbonates, oxides, and monosulfide minerals. HF treatment, a well-established experimental standard, dissolves the silicates from organic-rich mudrocks (Saxby 1970; Durand and Nicaise 1980; Robl and Davis 1993). Saxby (1970) mainly used chemicals such as HCl, HF, nitric acid (HNO_3), lithium aluminum hydride (LAH), sodium borohydride, and a mixture of zinc and HCl. In the chemical isolation method, Love (1982) suggested that "washing" is an important step in the experiment to remove all dissolved calcium ions.

Vandenbroucke (2003) performed a complete kerogen isolation using the Kerogenatron in Institut Francais du Petrole, France. This equipment is designed to isolate pure kerogen using solvent extraction and acidification under a nitrogen atmosphere. The procedure of the isolation was actually based on the steps constructed by Forsman and Hunt (1958), Saxby (1970), and Durand and Nicaise (1980). However, Vandenbroucke (2003) did not

manage to remove pyrite from the organic-rich mudrock sample. In a more recent study, Song et al. (2012) reported that the kerogen isolation technique can be improved by ultrasonic treatment with 40% HF at 60°C for 5 hours. The kerogen content isolated from the oil shale is increased as the concentration of the HF acid was increased.

Many studies, outlined in this subjection, have successfully isolated kerogen by applying this method. The main advantages of chemical isolation methods are they give a high kerogen recovery rate with little alterations of its chemical structure (Goklen et al. 1984; Zhao et al. 2013). Maintaining the chemical integrity of the kerogen helps to approach the in situ condition as closely as possible. The main disadvantage is the possibility of being exposed to hazardous chemicals such as DCM, benzene, HCl, and HF.

After successive physical treatments and rigorous chemical isolation of the organic-rich mudrock, pyrite is still embedded in the kerogen sample (Vandenbroucke 2003). The presence of pyrite in the organic matter will impact the electrical resistivity of the samples. Previous experiments have been introduced to remove pyrite from the extracted kerogen (Reaves 1984; Canfield et al. 1986; Tuttle et al. 1986). The use of HNO_3 (Saxby 1970; Ballice 2004; Ballice 2006) and LAH (Goklen et al. 1984) could chemically dissolve pyrite from the sample, despite the fact that the kerogen may be oxidized or nitrated. HNO_3 treatment also alters the kerogen to a non-condensable lower molecular weight compound (Robinson 1969; Al-Harahsheh et al. 2009). The most successful technique to remove

pyrite was proposed by Acholla and Orr (1993), who managed to eliminate up to 99% of pyrite using acidic chromium chloride ($CrCl_2$) solution.

The next subsection explains the impact of the kerogen isolation from organic-rich mudrocks on the geochemical properties obtained from Rock-Eval pyrolysis.

1.1.3 The Impact of Kerogen Isolation on Geochemical Properties

Katz (1983) reported that kerogen isolation can strongly affect the total organic carbon (TOC), T_{max}, and hydrogen index (HI) of the sample. HI is attributed to the amount of hydrogen in the kerogen. This is mainly because of the mineral matrix effect (Peters 1986; Spiro 1991). The mineral matrices in the organic-rich mudrock sample can react with the organic materials and dilute the relative concentration organic matter. This dilution yields a retention effect of the minerals, which reduces the capacity of the organic-rich mudrock to generate hydrocarbon and consequently lowers the S2 and hydrogen index (HI) compared to the isolated kerogen samples (Katz 1983; Peters 1986; Rojas et al. 2011). S2 is defined as the amount of hydrocarbons generated during the pyrolysis of kerogen between 300°C and 650°C. Although it is not always the case, the discrepancy of geochemical parameters between the mudrock and isolated kerogen samples might mislead the interpretation of the thermal maturity of the sample.

Geochemical parameters such as T_{max} and HI can be used as the indicator of thermal maturity. T_{max} values, which are obtained from the S2 peak during the second phase of

pyrolysis, may not be accurate for samples that have S2 lower than 0.2 mg HC/g (Peters 1986). Thus, solely relying on T_{max} to determine the thermal maturity of the sample is often not reliable for highly-mature samples. The HI values can validate the T_{max} prediction on thermal maturity of the samples. The hydrogen richness decreases as the maturity of the sample increases, which consequently drops the HI value. Therefore, in addition to T_{max}, HI is a good indicator for thermal maturity of the sample (Peters 1986; Dellisanti et al. 2010; Rojas et al. 2011; Nordeng 2012).

1.1.4 The Impact of Highly Mature Kerogen and Pyrite on Electrical Resistivity of Organic-Rich Mudrocks

Over recent decades, publications showed that the presence of connected networks of highly mature kerogen and pyrite can influence electrical resistivity measurements in organic-rich mudrocks (Passey et al. 1990; Chen et al. 2014; Kethireddy et al. 2014). It has been numerically proved that kerogen impacts the resistivity of organic-rich mudrocks. Kethireddy et al. (2014) successfully simulated a synthetic model and showed that the electrical resistivity of kerogen in the rock should not be ignored. Other factors that impact the effective electrical resistivity of organic-rich mudrocks are the connectivity of the kerogen network (Chen et al. 2013) and the volumetric concentration and electrical resistivity of the kerogen (Kethireddy et al. 2014). Neglecting the presence of conductive kerogen can lead to a 23% overestimation of water saturation estimated using conventional resistivity-porosity-saturation models (Kethireddy et al. 2014).

Several other studies indicated that the increase of kerogen maturity in organic-rich mudrocks increases the electrical resistivity of the rock (Passey et al. 1990; Shabro et al. 2011; Shabro et al. 2014). The presence of mature kerogen in organic-rich mudrocks decreases the effective porosity that is saturated by conductive saline water and, consequently, increases the electrical resistivity (Schmoker and Hester 1990; Shabro et al. 2011). This statement is in line with the result shown by Shabro et al. (2014), who introduced a technique of quantifying the impact of mature kerogen on the effective electrical resistivity by applying a parallel conductive path in the pore-scale numerical simulations.

Passey et al. (2010) inferred that the presence of pyrite in organic-rich mudrocks may reduce the electrical resistivity measurements, which consequently, may lead to unreliable interpretation of physical rock properties (Kennedy 2004; Clennell et al. 2010). Chen et al. (2014) inferred that considering pyrite connectivity can improve water saturation estimates up to 35% in direction with higher connectivity of pyrite network. However, pyrite may not be the only reason attributed to this condition.

Laboratory measurements was performed to observe the impact of thermal maturity on electrical resistivity of organic-rich mudrocks. The measurements of electrical resistivity are anomalously low for highly matured oil shale (Rajeshwar et al. 1979; Rajeshwar et al. 1980; Duba 1983; Meng et al. 2012) and coal char (Duba 1977). The main reason for these phenomena is still not fully understood. According to Rajeshwar et al. (1979), the decrease

in electrical resistivity of Green River oil shale when temperature increases, was attributed to structural changes and chemical transformations of the kerogen. This finding was confirmed by Rajeshwar et al. (1980) and Duba (1983), whose experiments suggest that the decreasing values of electrical resistivity of oil shale occur when kerogen is thermally decomposed, thus, leading to a relative increase of free carbon content. A similar trend was also observed in coal and coal char samples, where the total carbon in the sample increased from 67% to 80% as it was heated to 600°C (Duba 1977). Recently, Meng et al. (2012) showed that the electrical resistance measured on Nong'an and Huadian oil shale samples decreased as the temperature was increased up to 842°C. The temperature increase causes the conductive materials in the rock to move faster, allowing the conductive capacity to increase.

Passey et al. (2010) suggested that if the maturity of shale-gas reservoirs becomes high, the organic matter in the rock could change into electrically-conductive graphite, which could substantially decrease the electrical resistivity of organic-rich mudrocks. As the heat treatment temperature rises, the volatile components gradually diminish and the increasing amount of graphite-like material in the sample ultimately creates a connection with each other and enables electric current to flow (Celzard et al. 1999). The transformation of kerogen to graphite-like material has been investigated by previous experimental work. X-ray diffraction (XRD) measurements can evaluate the degree of graphitization as the organic-rich mudrock sample is synthetically matured (Harrison 1979; Daniels et al. 2007). Transmission Electron Microscopy (TEM) is also capable of

detecting structural transformation of kerogen towards graphite-like material with increasing thermal maturity (Daniels et al. 2007; Walters et al. 2014; Buseck and Beysacc 2014).

1.2 Statement of the Problem

Previous studies showed that volumetric concentration of kerogen (Chen et al. 2013; Kethireddy et al. 2014) and the connectivity of the kerogen and pyrite networks (Chen et al. 2014) can influence the electrical resistivity of the rock. The complex distribution and pore structure, various electrical resistivity of formation water, mature kerogen, and pyrite in organic-rich mudrocks create uncertainties upon interpreting the electrical resistivity logs for the assessment of fluid saturation.

Meanwhile, conventional resistivity-porosity-saturation models (e.g., Archie, Dual-Water, and Waxman-Smits) do not take into account the aforementioned complex physical rock properties of organic-rich mudrocks upon correlating the electrical resistivity and the fluid saturation. These models consider formation water as the only conductive component in the rock. This assumption is not reliable in organic-rich mudrocks due to the presence of highly mature kerogen and pyrite, which may have an impact on the electrical resistivity measurement of the rock (Passey et al. 2010). Thus, merely relying on conventional resistivity-porosity-saturation models might cause erroneous assessments of fluid saturations in organic-rich mudrocks, which leads to unreliable reserve evaluation.

However, an accurate measurement of electrical resistivity of isolated kerogen in the laboratory has yet to be accomplished. The lack of quantitative information regarding the values of electrical resistivity of kerogen, its electrical behavior due to temperature change, and its coexistence as well as connectivity with pyrite provokes difficulties in interpreting electrical resistivity logs for assessment of hydrocarbon saturation. Furthermore, the role of graphite-like material on electrical resistivity measurements in mature organic-rich mudrocks remains arguable. To address this problem, a comprehensive experimental approach was required to investigate the electrical resistivity behavior of kerogen isolated from organic-rich mudrocks and its chemical transformations as thermal maturity increases. The next subsection outlines the specific research objectives and gives in-depth explanation regarding the proposed method to isolate kerogen from organic-rich mudrocks and measure its electrical resistivity.

1.3 Research Objective

The main objective of this research is to:

- Measure electrical resistivity of isolated kerogen and organic-rich mudrock sample at different maturity levels.

To accomplish this objective, this research involves a series of laboratory experiments that include the combination of physical and chemical methods for kerogen isolation from organic-rich mudrocks, sample molding, synthetic maturation, micro computed tomography (CT) scan, TEM imaging, geochemical characterization, and the

measurement of electrical resistivity of the kerogen. These procedures are explained in detail in the next section.

CHAPTER II

KEROGEN ISOLATION AND GEOCHEMICAL CHARACTERIZATION

This chapter explains the experimental techniques used to isolate kerogen and characterize its geochemical properties (e.g., TOC, Tmax, and HI) of rock samples from Haynesville shale. The first step of the experimental work was to isolate kerogen organic-rich mudrocks using physical and chemical methods and remove pyrite from the core samples taken from the Haynesville shale. The physical method involved successive crushing and sieve meshing of the prepared core samples. The chemical isolation technique consisted of two main procedures, which were bitumen removal and acid demineralization on the shale samples. This process used a solvent extractor such as chloroform to extract bitumen from the samples. In the acid demineralization procedure, the experiment used HCl and HF to dissolve carbonates and silicates, respectively. To remove pyrite from the isolated kerogen powder, the experiment in this research used acidic $CrCl_2$ that was agitated in a series of glass flasks inside a nitrogen atmosphere glove box.

The original mudrock and kerogen samples were then crushed and prepared for further treatments and laboratory measurements, such as synthetic maturation, X-Ray fluorescence (XRF), Rock-Eval pyrolysis, micro computed tomography (CT) scan, and TEM imaging. The geochemical properties of the mudrock and isolated kerogen at different maturity levels were obtained from XRF measurements and Rock-Eval pyrolysis. The success of the kerogen isolation experiment can be measured using XRF, which

compares the result before and after the kerogen isolation, as well as after the pyrite removal experiment.

2.1 Kerogen Isolation

In this thesis, three techniques were employed together to isolate kerogen from organic-rich mudrock samples. The first technique employed a physical method, which involved rigorous rock crushing and passing the crushed sample through a sieve shaker. Sample grains that passed through the sieve of 170 mesh (88 μm) were collected to undergo the chemical method, which involved solvent extraction, acid demineralization, and sample washing. These physical and chemical processes aimed to remove bitumen or moveable hydrocarbon, carbonates, and calcites from the organic-rich mudrock. However, pyrite still remained in the sample, which impacts the electrical resistivity measurement. Therefore, the sample was treated with $CrCl_2$ solution in a nitrogen atmosphere to remove pyrite.

Previous studies indicated that the combination of physical and chemical methods to isolate kerogen has been proven to obtain optimum recovery rate of kerogen without changing its chemical structure (Forsman 1963; Saxby 1970; Durand and Nicaise 1980; Vandenbroucke and Largeau 2007). **Figure 1** shows the workflow of the twelve steps of the kerogen isolation procedure, which includes both the physical and the chemical methods.

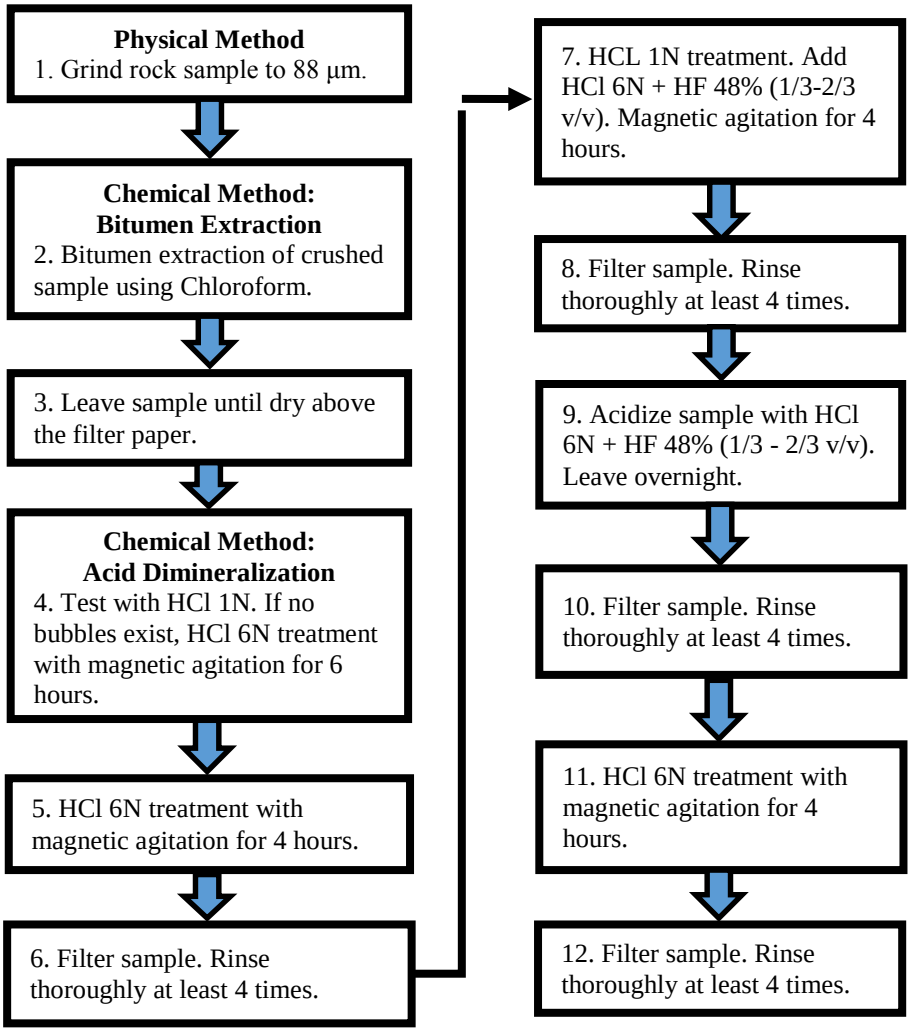

Figure 1: The workflow of physical and chemical methods of kerogen isolation from organic-rich mudrock samples.

2.1.1 Physical Method

The first step of the physical method was repetitively crushing the organic-rich mudrock sample. This step corresponds to step one in Figure 1. Exhaustively crushing the rock sample was important since particle size impacted the efficiency of the chemical isolation method. Smaller particle size increased the surface area per unit volume of the sample,

which exposed more sites for the chemicals to extract bitumen and to demineralize non-organics from the rock matrix.

Steel mortar and pestle were used to crush the organic-rich mudrock sample, as shown in **Figure 2a**. The next step was to place the crushed sample in the sieve and turn it on for 300 seconds. The rock sample that falls below the sieve of 170 mesh (88 μm) was fine enough to undergo the chemical isolation methods. All of the remaining grains were gathered and treated for another round of crushing (**Figure 2b)**. This physical treatment was repeated until at least 30 g of sample is gathered to start the chemical isolation methods.

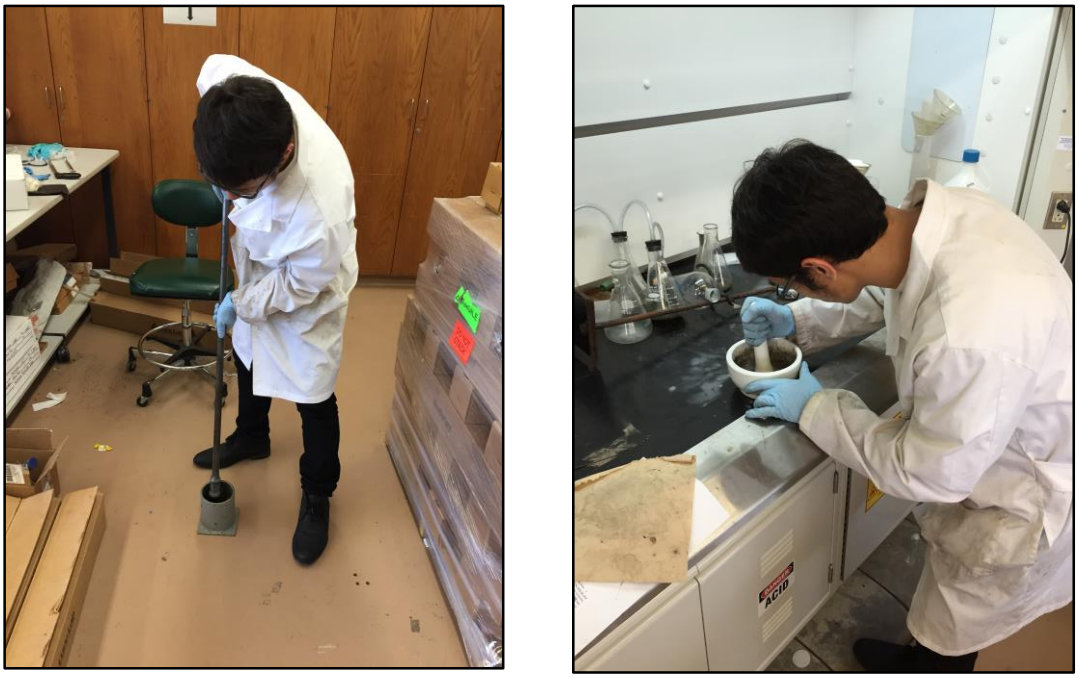

a b

Figure 2: Repetitive and thorough crushing of the mudrock sample using (a) steel mortar and pestle and (b) ceramic mortar and pestle.

2.1.2 Chemical Method

To remove soluble bitumen from the samples, this experiment used chloroform. Then the carbonates, silicates, feldspars, and clays were dissolved using the combination of HCl and HF. Furthermore, thoroughly rinsing the sample after each acid treatments was important to remove all dissolved minerals without causing further chemical reaction within the samples. The next segment presents the details of each step in the chemical isolation method.

2.1.2.1 Solvent Extraction

Chloroform has been widely used as an organic solvent to extract soluble bitumen from organic-rich mudrock samples (McIver 1962; Durand and Nicaise 1980; Lis et al. 2008; Al-Harasheh 2010; Zhao et al. 2013). Solvent extraction was conducted in a 400 ml glass beaker above a magnetic spinner in ambient temperature. 30 g of sample was agitated with chloroform using the magnetic spinner for thirty minutes. The magnetic spinning agitation technique made sure that all grains were exposed to chloroform.

Then the beaker was placed in an ultrasonic bath. The ultrasonic treatment of the shale sample used 42 kHz of frequency and 100 W of power. After thirty minutes of ultrasonic treatment, the sample was taken out and re-agitated with the magnetic spinner. This method was repeated at least twice. The separation of aggregates of solid particles occurred because of four additive effects: interface, perturbation, turbulence, and cumulative energy effects (Zhao et al. 2013). These effects enhanced the ultrasonic capillary effect and accelerated the separation of organics.

The next step was decanting the chloroform through a filter paper. The remaining material above the filter paper was ready for the acid treatment. **Figure 3** shows the workflow of the solvent extraction process.

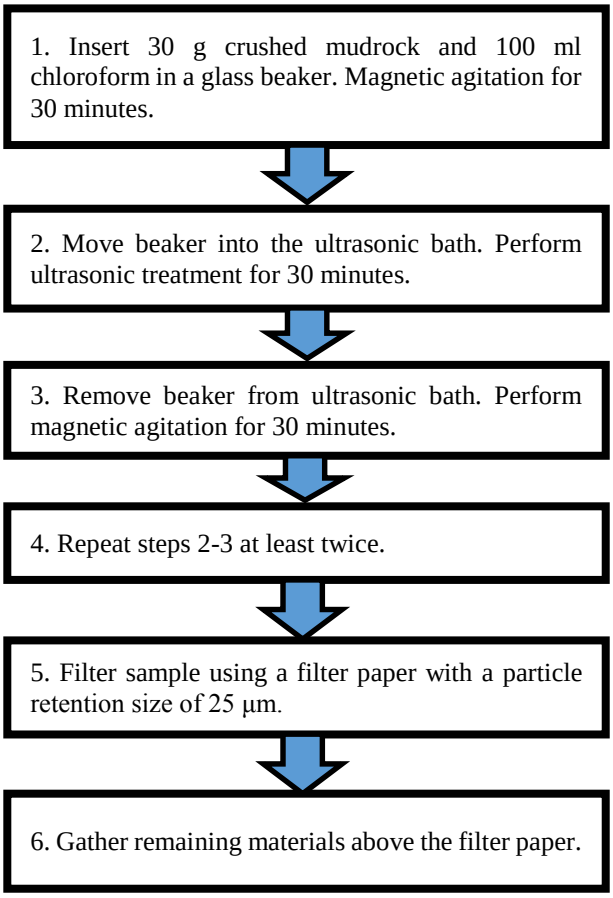

Figure 3: Experiment steps of the bitumen removal from the organic-rich mudrock sample.

2.1.2.2 HCl Treatment

The HCl treatment was used to dissolve the carbonates, sulfides, sulfates, and hydroxides from organic-rich mudrocks. This procedure was conducted at room temperature to avoid

maturation and subsequent structural alteration of kerogen. The first step of the HCl treatment was to mix 20 ml of 1N HCl with 30 g shale sample inside a 400 ml polyethylene beaker (**Figure 4)**. HCl immediately dissolved calcium carbonate ($CaCO_3$) in the shale sample, which created bubbles in the beaker (**Figure 5)**. To prevent excessive bubbling, HCl was poured slowly into the beaker while the sample was stirred. Then the sample was agitated above the magnetic spinner with an addition of 50 ml 6N HCl for 6 hours. The main chemical reaction that occured during the HCl treatment was as follows:

$$CaCO_3(s) + 2\ HCl(aq) \longrightarrow CaCl_2(aq) + CO_2(g) + H_2O(l).$$

The calcium chloride ($CaCl_2$) produced from this reaction was soluble in water and dissociated to form calcium (Ca^{2+}) and chloride (Cl^-) ions.

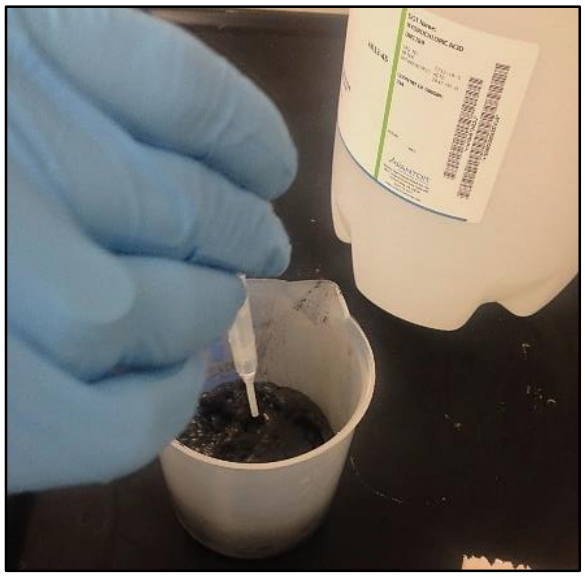

Figure 4: Adding HCl to sample in beaker. This step dissolves the carbonates that was present in the organic-rich mudrock sample.

Figure 5: Bubbling occurred as HCl dissolved the carbonates in the sample.

2.1.2.3 Sample Rinsing and Filtering

The chemical reaction that occurred during the HCl treatment released Ca^{2+} ions, which react easily with fluoride (F^-) ions during HF treatment, producing calcium fluoride (CaF_2). This fluoride compound was difficult to dissolve once it precipitates. To avoid the forming of CaF_2, it was important to perform thorough rinsing of the decarbonized mudrock sample, particularly after step 5, to wash out all of the calcium ions. In every rinsing procedure, the sample was filtered using a VWR qualitative filter paper 415 with a particle retention of 25 μm. Sample rinsing was repeated until the color of the filtrate was the same as the water. In this condition, it was assumed that the pH of the filtrate was the same as the pH of the water and free of calcium ions. **Figure 6a** and **Figure 6b** show

the filtering and rinsing processes that were performed after the HCl treatment. After the fourth rinse, the sample should not be allowed to dry completely to prevent oxidation and sample sticking on the filter paper.

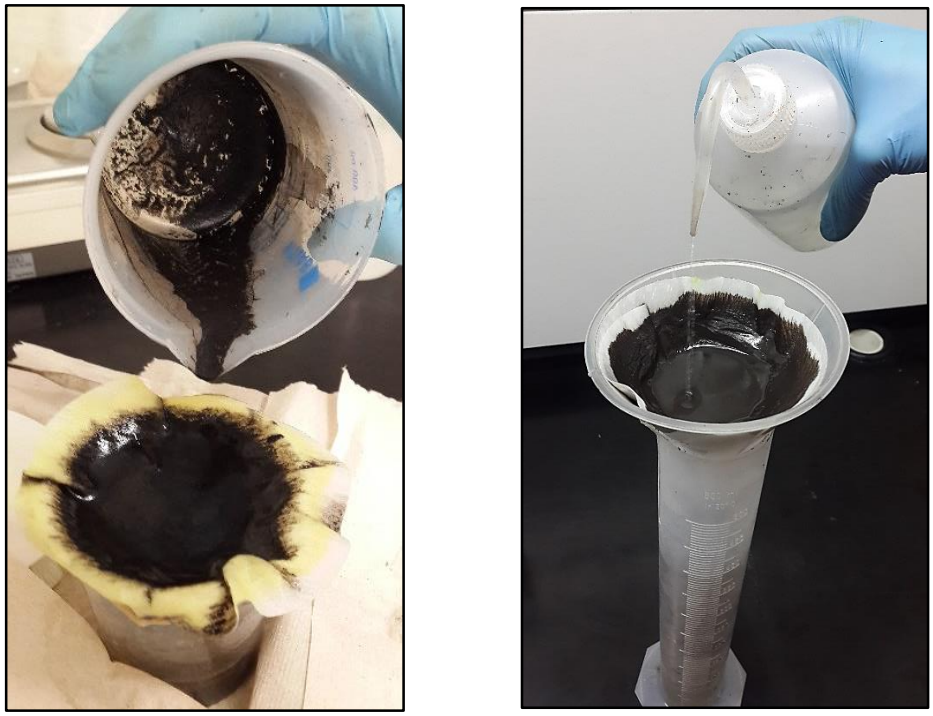

(a) (b)

Figure 6: After the HCl treatment, the experiment proceeds to (a) filtration of the sample using VWR qualitative filter paper 415 followed by (b) repetitive rinsing using deionized water.

2.1.2.4 HF Treatment

Prior to the HF treatment, the sample was mixed with 10 ml of 1N HCl in the beaker. If no bubbling occurred, a mixture of 6N HCl and HF 48% (1/3-2/3 v/v) was added in the beaker. The main objective of HF treatment was to dissolve the silicates that remain in the powdered sample. Adding HCl into the mixture accelerated the chemical reaction to

dissolve the silicates. The main chemical reaction that occurred during this process is given by

$$4\,HF + SiO_2 \longrightarrow SiF_4 + H_2O.$$

HF was poured slowly into the beaker to maintain safe experimental conditions and to control the creation of bubbles (**Figure 7**). When no more bubbles are visible, the sample was agitated with the magnetic spinner for 4 hours. The next step was to carefully rinse the sample at least four times and repeat the HF treatment one more time. After the second HF treatment, subsequent rinsing was performed, then the sample was ready for the last HCl treatment.

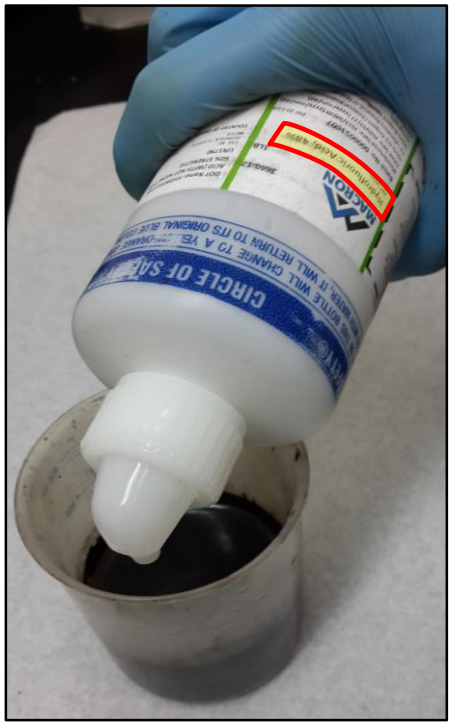

Figure 7: Pouring HF into the sample. In this step, HF dissolved the silicates in the decarbonized sample. During this process, HCl was also added to accelerate the chemical reaction of dissolving the silicates.

2.1.2.5 Second HCl Treatment

The experiment continued to the last acid treatment which used 6N HCl. The rinsed decarbonized and silicate-free sample was placed inside a 400 ml polyethylene beaker. 30 ml of 6N HCl was added while stirring the sample intermittently. At this stage, there should not be any visible bubbling as all the carbonates and silicates have been dissolved. This procedure was important to eliminate all the remaining ions that might form to an insoluble fluoride compound upon drying the sample. This procedure takes four hours of magnetic agitation before the final rinsing. In the end, the sample was stored inside a beaker and left to dry.

2.1.3 Pyrite Removal

After successive physical treatments and rigorous chemical isolation of the organic-rich mudrock, pyrite was still embedded in the kerogen sample. XRF results (Chapter IV) proved that iron (Fe) was present in the kerogen sample. In this research, pyrite elimination was required to investigate the electrical resistivity of pyrite-free kerogen samples. To remove pyrite, acidic $CrCl_2$ solution was used, as proposed by Acholla and Orr (1993).

The chemical reaction that occured during the pyrite removal experiment is given by

$$FeS_2\,(s) + 2CrCl_2\,(aq) + 4HCl\,(aq) \longrightarrow FeCl_2\,(aq) + 2CrCl_3\,(aq) + 2H_2S\,(g).$$

The acidic $CrCl_2$ solution disintegrates pyrite (FeS_2) and produces iron chloride ($FeCl_2$) and sulfuric acid (H_2S). To prevent oxidation of $CrCl_2$, the experiment was conducted under a nitrogen atmosphere. To this end, a nitrogen chamber –a sealed container box with

rubber gloves arranged in such a way for performing tasks inside the box without breaking containment– was successfully constructed. **Figure 8** depicts the procedures employed for pyrite removal in this thesis.

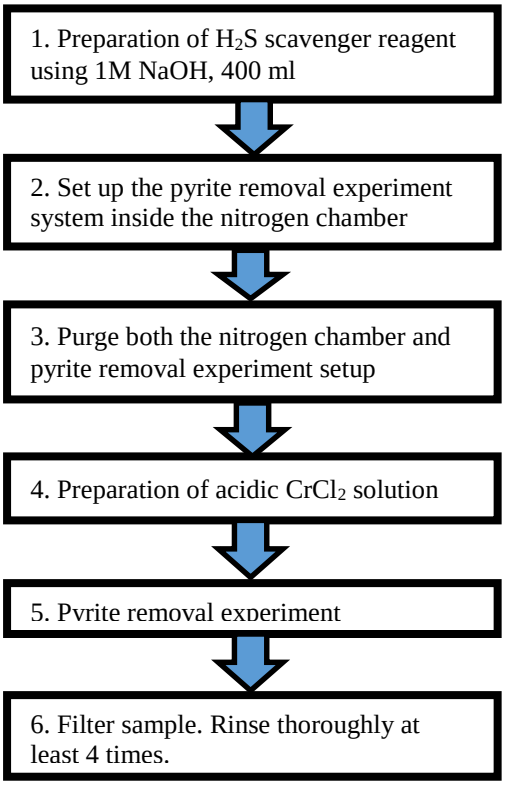

Figure 8: The workflow of pyrite removal experiment from kerogen-pyrite mixture sample.

2.1.3.1 Preparation of H_2S Scavenger

Pyrite removal experiment produced H_2S gas as a product of separating pyrite from the kerogen-pyrite mixture sample. H_2S is colorless, extremely corrosive, poisonous, flammable, explosive, and hazardous if exposed to the atmosphere. Therefore, it was important to perform the pyrite removal experiment inside a fume hood and prepare H_2S

scavenger solution. The H_2S scavenger solution captured H_2S gas and prevent it from being released to the atmosphere. This experiment used 1M of sodium hydroxide (NaOH) in a 400 ml solution as the H_2S scavenger, placed in a 500 ml Erlenmeyer glass flask. In order to dilute 1M NaOH for 400 ml solution, 16 g of NaOH pellets were mixed with 392.5 ml water. Three flasks of 1M NaOH – 400 ml solution were prepared for the pyrite removal experiment setup.

2.1.3.2 Pyrite Removal Experiment Setup

Figure 9 shows the pyrite removal experiment setup, which was placed inside the nitrogen chamber. The main function of the cone-shape separatory funnel (**Figure 9a**), which was clamped by the iron ring stand (**Figure 9b**), was to insert the acidic $CrCl_2$ solution and HCl into the primary Erlenmeyer flask (**Figure 9c**), where the pyrite removal reaction was conducted. Downstream of the primary Erlenmeyer flask was a series of three more Erlenmeyer flasks (**Figure 9d**) that were connected to each other by flexible tubes (**Figure 9e**). Each of these three flasks contained 1M NaOH – 400 ml solution, which was the H_2S scavenger. The NaOH solution captured the produced H_2S gas from the pyrite removal experiment. To prevent H_2S from leaking, all Erlenmeyer flasks are attached by rubber stoppers (**Figure 9f**) that had holes for inserting the flexible tubes. **Figure 9g** was the nitrogen line that connects to the primary Erlenmeyer flask. The magnetic stirrer (**Figure 9h**) that rotated the spinner bar (**Figure 9i**) was placed under the primary Erlenmeyer flask, providing agitating motion of the kerogen sample. **Figure 10** shows the pyrite removal experimental setup as the pyrite removal experiment was in progress.

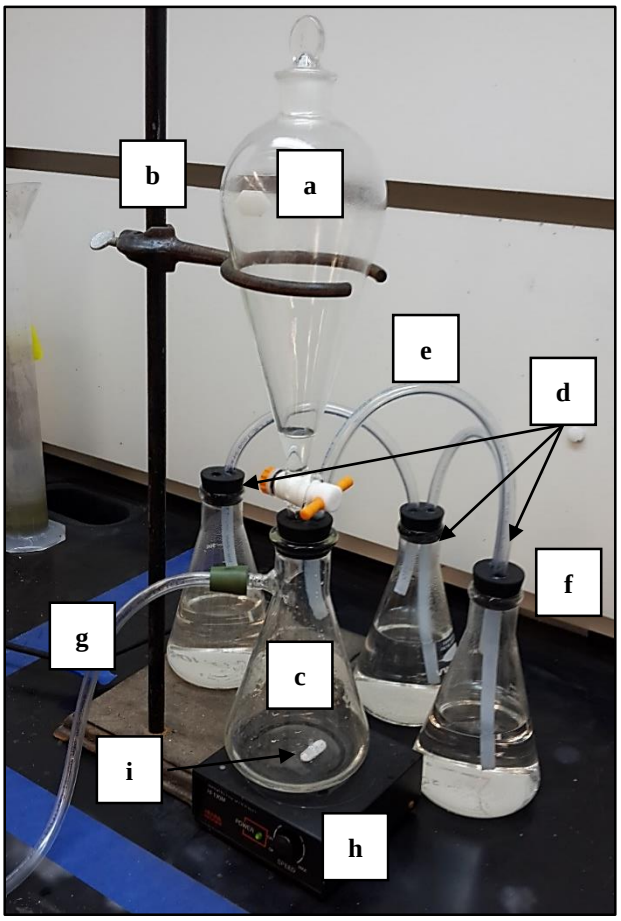

Figure 9: Pyrite removal experiment setup which includes: (a) coned-shape separatory funnel, (b) iron ring stand and clamp, (c) primary Erlenmeyer flask, (d) a series of Erlenmeyer flasks with NaOH, (e) flexible tubes, (f) rubber stopper, (g) nitrogen input for the pyrite removal setup, (h) magnetic stirrer, and (i) magnetic spinner bar.

Figure 11 shows the nitrogen chamber for the pyrite removal experiment. The nitrogen chamber was designed in such a way to have enough space for performing the pyrite removal experiment, such as diluting the acidic $CrCl_2$, transferring chemical solution from one flask to another, rinsing, and filtering. This chamber has three input holes (**Figure 11a** and **Figure 11b**), two of which were for inserting the nitrogen lines (i.e., for injecting nitrogen gas into the pyrite removal setup and the chamber), and the other input was for

inserting the magnetic stirrer cable. The corresponding output holes (**Figure 11c** and **Figure 11d**) were designed to prevent nitrogen pressure building up in the setup or in the chamber. The rubber gloves were designed to attach on the sidewall of the chamber, 25.4 cm from the bottom (**Figure 11e**). A rubber seal, attached to the bottom of the chamber, prevented nitrogen to leak (**Figure 11f**).

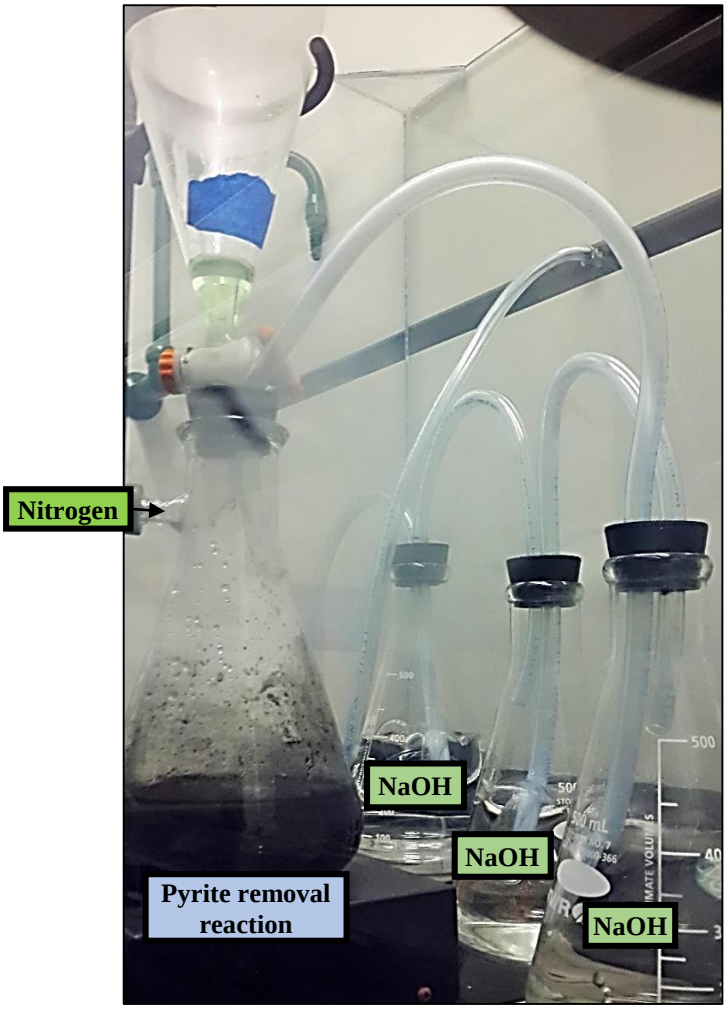

Figure 10: Pyrite removal experiment from kerogen-pyrite mixture sample occurred inside the primary Erlenmeyer flask. The nitrogen flow prevented the acidic $CrCl_2$ solution from oxidation and ensured the H_2S gas that comes out from the pyrite removal reaction flows downstream was trapped by the NaOH solution.

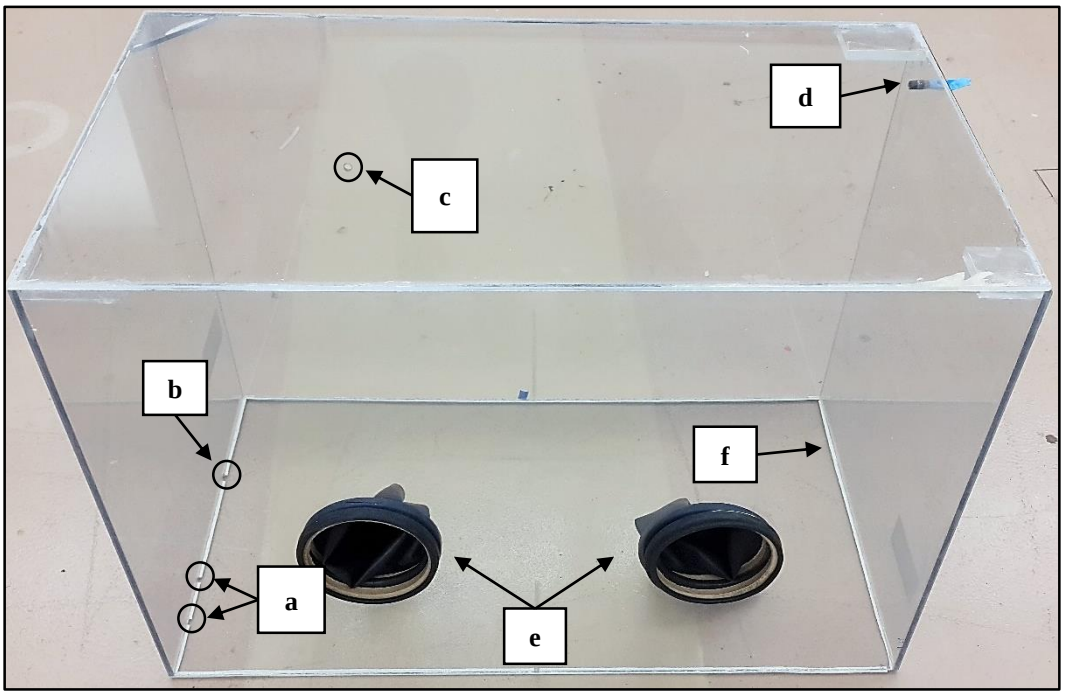

Figure 11: The nitrogen chamber designed for pyrite removal experiments which includes: (a) two nitrogen input holes, (b) cable input hole, (c) nitrogen output hole for the pyrite removal experiment setup, (d) nitrogen output hole for the chamber, (e) rubber gloves, and (f) rubber sealed bottom.

2.1.3.3 Nitrogen Line and Setup Purging

Purging the nitrogen chamber and the experiment setup was the next step. Since $CrCl_2$ easily reacts with oxidizing agents, the chamber and experiment setup was purged completely from oxygen. In this step, both the chamber and pyrite removal experiment setup were purged for approximately 10 to 15 minutes with 20 psi of nitrogen gas. Regulating the pressure above 20 psi might cause pressure to build inside the setup faster than it bleeds, which may harm the integrity of the chamber and the pyrite removal experiment setup. There was no leak detected from either the nitrogen chamber or the pyrite removal setup.

2.1.3.4 Preparation of Acidic $CrCl_2$ Solution

The next step was to prepare 1M $CrCl_2$ – 50 ml solution inside the chamber. 6.145 g of 97% anhydrous $CrCl_2$ was diluted with 47.8 ml of water in a 400 ml polypropylene beaker. The green $CrCl_2$ solution was then mixed with 30 ml of 0.5M HCl. This acidic $CrCl_2$ solution was poured in the separatory funnel (**Figure 12**).

Figure 12: Acidic $CrCl_2$ solution inside the coned-shaped separatory funnel.

2.1.3.5 Pyrite Removal Experiment

Prior to starting the pyrite removal experiment, 5 g of kerogen-pyrite mixture powder sample was placed inside the primary Erlenmeyer flask, and mixed with 20 ml of ethanol. Adding ethanol was a treatment to wet the sample so that good contact between the acid and rock was achieved (Robinson 1969). While the nitrogen was continuously flushing the experiment setup, the acidic $CrCl_2$ solution was added drop-by-drop into the primary Erlenmeyer flask. The next step was to add 40 ml of concentrated HCl (13M) into the primary Erlenmeyer flask through the separatory funnel. The sample was agitated for two hours.

2.1.3.6 Sample Rinsing and Filtering

After pyrite removal treatment, the sample was passed through a VWR qualitative filter paper 415 and collected in a funnel (**Figure 13a**). The next step is shown in **Figure 13b**, where the sample was rinsed with water at least four times until the filtrate was neutral. The next step is to wait until the isolated pyrite-free kerogen sample was dry.

2.2 Elemental Analysis

This research employed elemental detection and analysis of all investigated samples using the XGT-7000 X-Ray Analytical Microscope from Horiba, which merges the features of optical observation and Energy Dispersive X-Ray Fluorescence (EDXRF) analyzer. In this process, the XRF measurement was performed three times: before kerogen isolation, after the first acid demineralization (first treatment), and after pyrite separation (second

treatment). The EDXRF analyzer was able to detect elements ranging from sodium to uranium and reaches a spatial resolution as low as 30 μm.

(a) (b)

Figure 13: The last two steps of the pyrite removal experiment, which include (a) filtering the sample on a filter paper in a funnel and (b) rinsing the isolate pyrite-free kerogen sample at least four times until the filtrate is neutral.

During the measurement, all of the consolidated molded samples was attached on a sample plate holder enclosed in a radiation safety enclosure. This thesis only reported the elements that were detected under the energy level of 15 keV, which include aluminum (Al), silicon (Si), sulfur (S), potassium (K), calcium (Ca), titanium (Ti), manganese (Mn), iron (Fe), and zinc (Zn). The EDXRF was able to generate an element map from a specific field of view in the sample. The element map showed the fluorescence intensity for each element

in the region under analysis. **Figure 14** shows an element map of calcium obtained from the mudrock sample, before the acid demineralization.

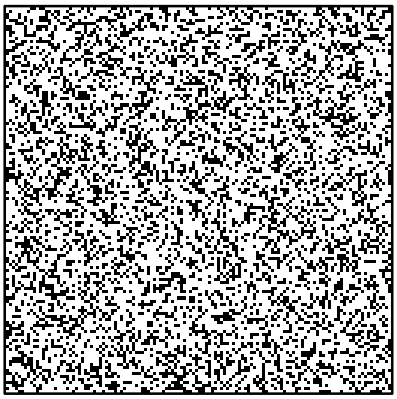

Figure 14: Element map of calcium from the Haynesville mudrock sample generated using the EDXRF analyzer.

The next step after XRF measurements was to perform synthetic maturation by heat-treating all the samples (i.e., original mudrock and isolated kerogen) in a vacuum condition. The samples were heat-treated with 5°C/min to temperatures of 150°C, 300°C, 425°C, 500°C, 650°C, and 800°C. The artificially matured samples were prepared for the Rock-Eval pyrolysis and electrical resistivity measurements. Chapter III explains the technique to prepare the powder samples and the technique for electrical resistivity measurements at different maturity levels.

2.3 Rock-Eval Pyrolysis

One of the most widely used techniques to investigate the thermal maturity and TOC of organic-rich mudrocks is the Rock-Eval pyrolysis. Using this method, the organic-rich

mudrock and isolated kerogen samples were heated under inert atmosphere of nitrogen. The Rock-Eval pyrolysis was performed in W.D. Von Gonten Laboratories, College Station, using the Rock-Eval 6 (**Figure 15**). This research employed two sets of pyrolysis procedures for (a) the organic-rich mudrock sample and (b) the isolated kerogen sample. In both procedures, the rock samples were finely ground to 125 μm and placed in a crucible for the pyrolysis.

Figure 15: Rock-Eval 6 used for Rock-Eval pyrolysis located at W.D. Von Gonten Laboratories, College Station, Texas.

The organic-rich mudrock pyrolysis procedure used 60 mg of the powdered mudrock sample. The first phase of the pyrolysis procedure started with maintaining the oven

temperature at 300°C for 3 minutes. At this temperature, free hydrocarbons were volatilized and recorded as the S1 curve. The second phase was heating the sample in the oven from 300°C to 650°C with a heating rate of 25°C/min. In this phase, the kerogen was volatilized and the hydrocarbons generated are measured by the Flame Ionization Detector (FID). The FID was able to detect organic compounds emitted during each stage of heating. During this step, the S2 curve was developed, which corresponds to the amount of hydrocarbons (mg) generated from the thermal cracking of kerogen in one gram of rock sample. The temperature at which S2 curve reached its maximum is called T_{max}. The third phase of the pyrolysis procedure was employed between 300°C and 390°C. In this phase, the carbon dioxide (CO_2) decomposed from the organic matter and the CO_2 mass (mg) per gram of rock sample was recorded by infrared detectors, as S3.

In the case of isolated kerogen pyrolysis procedure, the required amount of isolated kerogen was 10 mg to avoid detector saturation. This procedure subjects the isolated kerogen sample to an increasing temperature ranging from 300°C to 800°C, with a rate of 25°C/min. The final temperature of the programmed pyrolysis was increased from 650°C to 800°C to avoid an incomplete pyrolysis of the isolated kerogen samples and to observe a complete S2 curve that returns to the baseline (Vandenbroucke and Largeau 2007).

The parameters obtained from Rock-Eval pyrolysis that describes the geochemical characterization of the sample are summarized in **Table 1**. The thermal maturity of each sample was inferred from the T_{max} and HI values (Peters 1986; Dellisanti et al. 2010; Rojas et al. 2011; Nordeng 2012).

Table 1: Parameters obtained from Rock-Eval pyrolysis that are used for geochemical characterization.

Parameter	Units	Description
S1	mg HC/g rock	Free hydrocarbons volatilized to at 300°C isotherm.
S2	mg HC/g rock	Hydrocarbons generated during the pyrolysis of kerogen between 300°C and 650°C (up to 800°C for the pure organic matter pyrolysis program) with a temperature gradient of 25°C/min.
S3	mg HC/g rock	Organic carbon dioxide released between 300°C and 390°C.
T_{max}	°C	Temperature at which the maximum amount of S2 hydrocarbons are generated during Rock-Eval pyrolysis.
TOC	wt %	A measure of the organic richness of a rock, i.e. the quantity of organic carbon (both kerogen and bitumen) in a rock sample.
HI	mg HC/g TOC	The ratio of hydrogen to TOC in the sample, defined as S2x100/TOC. HI is attributed to the amount of hydrogen in the kerogen.
OI	mg CO_2/g TOC	The ratio of CO_2 to TOC in the sample, defined as S3x100/TOC. OI is attributed to the amount of oxygen in the kerogen.

2.4 TEM Imaging

TEM was used to observe structural planes of the powdered mudrock and isolated kerogen samples at the atomic level. This microscope used a broad beam of electrons that passed through a thin sample producing an image due to diffraction. The TEM images were obtained from the Microscopy Imaging Center at Texas A&M University using the FEI Tecnai G2 F20 ST, as shown in **Figure 16**. In this thesis, the main objective of using the TEM was to identify the presence of graphite-like materials in the thermally matured kerogen sample. The TEM equipment was operated at 200 kV using S-twin objective lens and equipped with a Gatan CCD 2k x 2k camera, an EDAX instrument EDS detector, and a Fischione ultra-high resolution STEM high angle annular dark field detector (HAADF). The samples for TEM imaging were prepared by the Microscopy Imaging Center, Texas

A&M University. Both mudrock and isolated kerogen powder were embedded to an epoxy. Micro-tomed sections were cut to 80 nm and put on 400 mesh copper grid. The grid was then coated with a 15 nm evaporated carbon and put under the microscope.

Figure 16: FEI Tecnai G2 F20 ST Microscope used for TEM images located at the Microscopy Imaging Center, Texas A&M University.

CHAPTER III

ELECTRICAL RESISTIVITY MEASUREMENTS

The previous chapter explains the techniques used to isolate kerogen. The mudrock and isolated kerogen sample were then measured for its electrical resistivity at different temperatures to which the sample was heated to, ranging from 25°C to 800°C. This chapter explains the experimental techniques in molding the kerogen and measuring electrical resistivity.

3.1 Kerogen Molding

The isolated kerogen sample obtained from the physical and chemical isolation procedures outlined in the previous chapter were collected for electrical resistivity measurements. The isolated kerogen sample was in powder form, which was difficult to measure its electrical resistivity. Therefore, this research implemented a technique to mold the powdered kerogen into a solid form. A specific mold frame was designed to compress the kerogen powder to create a consolidated isolated kerogen disk, as shown in **Figure 17.** The molding equipment and the procedures to mold the isolated kerogen are explained in the following subsections.

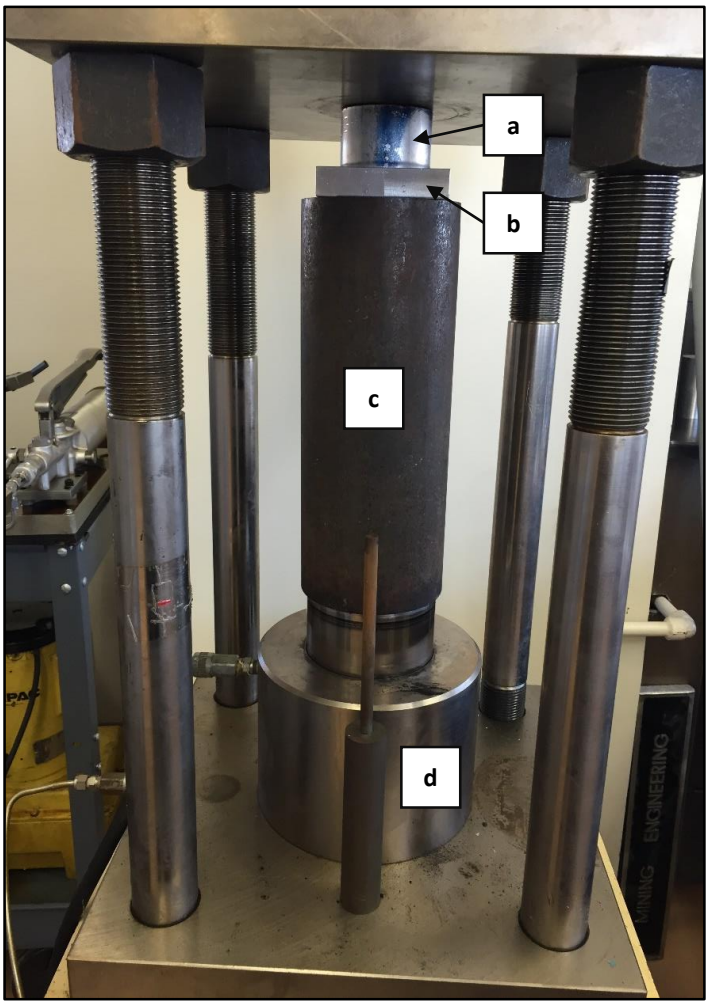

Figure 17: The designed molding system includes: (a) aluminum compressing rod, (b) squared base frame, (c) aluminum cylinder beam, and (d) hydraulic load frame.

3.1.1 Equipment

The following subsections explain the details of each piece of equipment in the molding system.

3.1.1.1 Aluminum Compressing Rod

Figure 18 is showing the molding device which is an aluminum compressing rod. The rod is a solid aluminum cylinder with a diameter of 6.35 cm at the bottom part and 8.9 cm at

the upper part. The bottom part of the compressing rod was flattened in order to produce a well consolidated and smooth surface of the isolated kerogen.

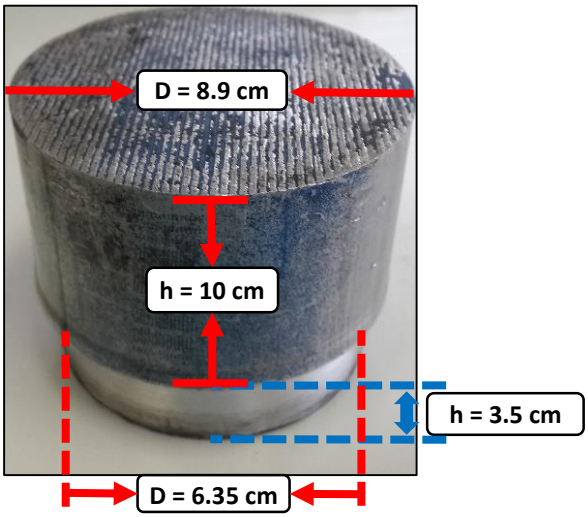

Figure 18: Aluminum compressing rod.

During the molding process, the isolated kerogen powder was placed inside a polyvinyl chloride (PVC) ring. Upon compression, the PVC ring assured the powder to be evenly consolidated and formed a good disk shape without breaking its perimeter. The inner diameter of the PVC ring is 2.54 cm and the thickness is 0.32 cm.

3.1.1.2 Square-Base Frame

The squared base frame was made of steel, as shown in **Figure 19a**. The height is 3.8 cm and hollowed in the middle with a 6.35 cm diameter, which allowed the sample to sit inside while compressed by the compressing rod. The base frame was designed to split in half, as shown in **Figure 19b**. This design helps to easily remove the sample from the

square-base frame after the compressing procedure, by loosening the two bolts that connected the two-piece frame.

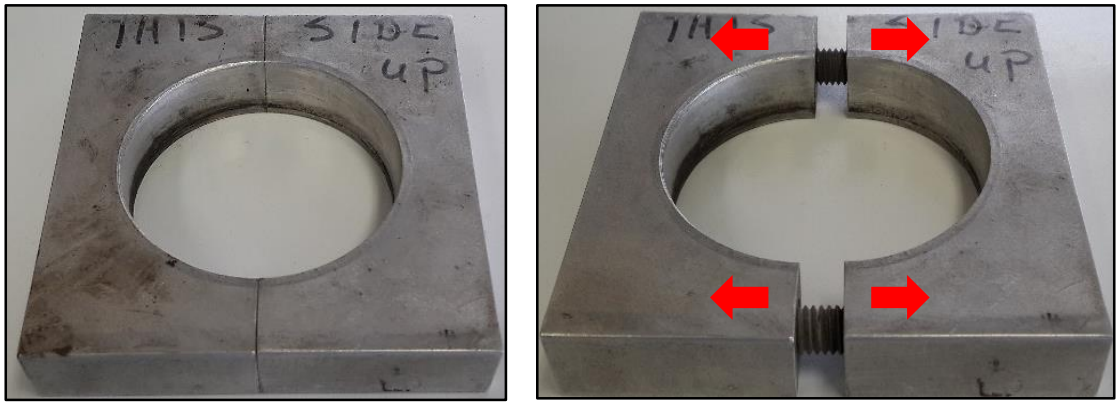

(a) (b)

Figure 19: Square-base frame when the two pieces (a) closed and (b) apart.

3.1.1.3 Aluminum Cylinder Beam

As shown in **Figure 20**, the aluminum cylinder beam is an intermediary equipment that sit between the aluminum compressing rod and the top part of the frame. It helped the hydraulic pump not to compress the load cell all the way to the top, which saves time and mitigate any possible failure to the hydraulic pump.

3.1.1.4 Hydraulic Load Frame

All of the aforementioned equipment were placed in the hydraulic load frame. The main function of the load cell was to lift the square-base frame and push it towards the top part of the frame. The hydraulic load frame was connected to an automatic hydraulic pump.

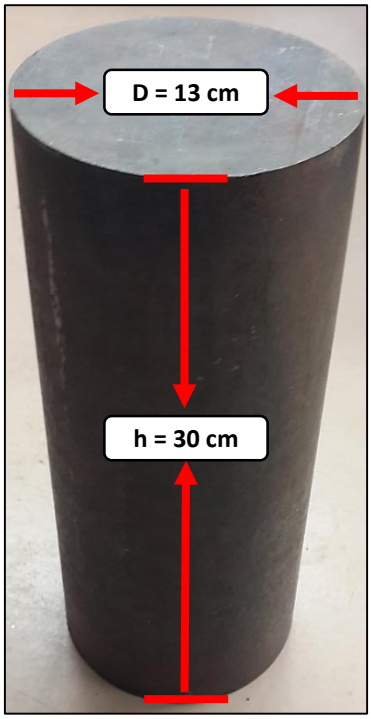

Figure 20: Aluminum cylinder beam.

3.1.2 Molding Procedure

The first step of the kerogen molding was to make sure that the surface of the load cell in the hydraulic load frame was clean, smooth, and flat. The main reason was to avoid any contamination to the kerogen and produce a smooth and well consolidated sample. The next step was to place the square-base frame on top of the load cell and put the PVC ring inside the hollowed part. Then, 30 mg of kerogen powder was placed inside the PVC ring. The aluminum compressing rod was then placed carefully above the sample and the PVC ring. The compressing treatment was ready after settling the aluminum cylinder beam above the compressing rod. Finally, the automatic hydraulic pump was turned on to lift the load cell, elevating all equipment therein. As the load cell was lifted towards the top

part of the frame, the aluminum cylinder beam gave compression force to the isolated kerogen sample underneath it. The compressing pressure were increased slowly until the automatic hydraulic pump cannot compress the sample any further (**Figure 21**). The last step was to pull out the molded isolated kerogen sample from the PVC ring.

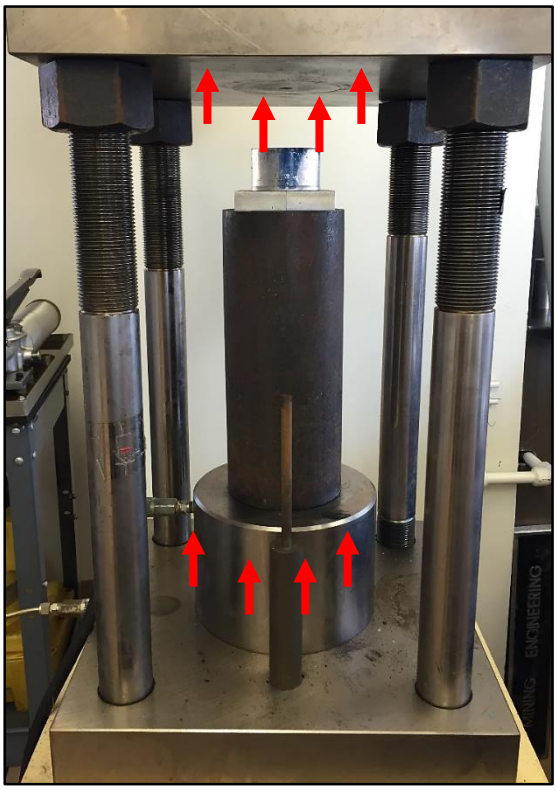

Figure 21: The process of molding the kerogen powder sample using an aluminum cylinder and a metal block frame with a 6.35 cm diameter hole. The samples were compressed using a hydraulic load frame.

3.2 Laboratory Measurements of Electrical Resistivity

In this research, the electrical resistivity of the molded kerogen is measured using a high resistance electrometer coupled with resistivity test fixture (**Figure 22**). The next

subsections show how the newly designed resistivity fixture worked and how to measure electrical resistivity of the molded sample.

3.2.1 Electrical Resistivity Measurement Equipment

The following subsections lists the specifications of the high resistance electrometer and the resistivity test fixture.

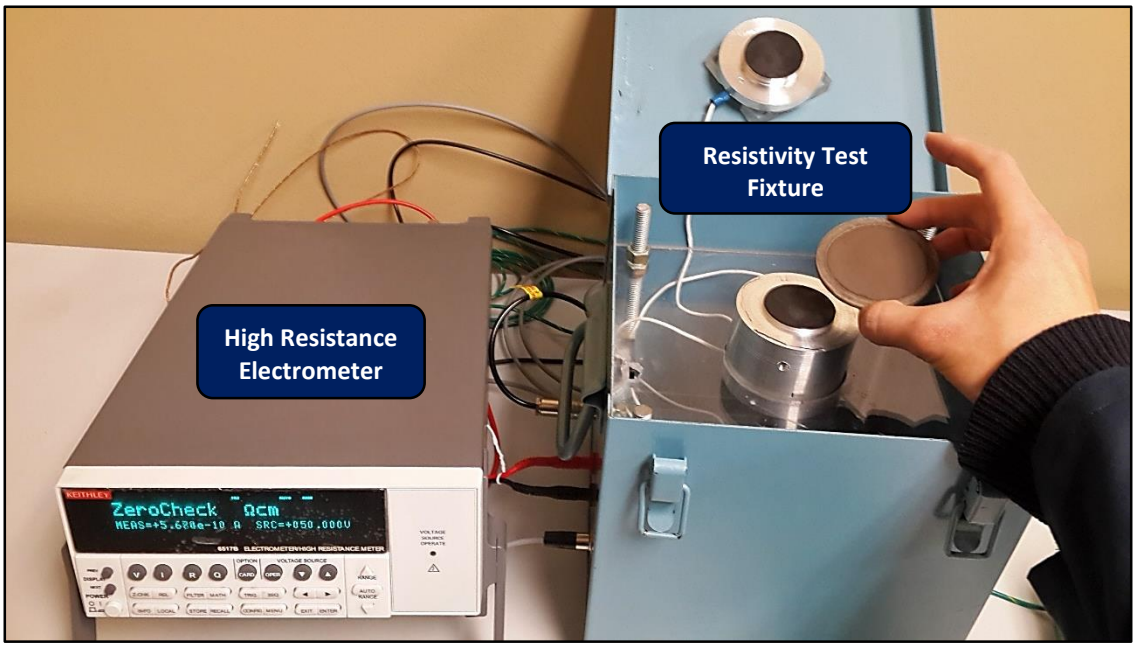

Figure 22: High resistance electrometer and the newly designed resistivity test fixture.

3.2.1.1 High Resistance Electrometer

This high resistance electrometer used in this thesis was the model 6517B Electrometer/High Resistance Meter from Keithley. The high resistance electrometer was able to measure electrical resistivity up to 10^{16} ohm-m. The electrical resistivity is defined

as the resistance of the sample multiplied by the cross-sectional area of the sample divided by the thickness of the sample. This device has a 5½-digit resolution and is able to measure the aforementioned electrical properties in the temperature range of -25°C to 150°C.

3.2.1.2 Resistivity Test Fixture

The resistivity fixture was capable of (a) measuring electrical resistivity of a solid and smooth-surfaced sample (b) accommodating sample sizes ranging from 2.54 cm to 10.16 cm in diameter and from 0.2 cm to 1.27 cm in thickness, and (c) operating in the temperature range of -25°C to 85°C. This device was connected to the high resistance electrometer using a three-lug triaxial connector to measure electrical resistivity of the sample, with an operating temperature between -30°C and 85°C. As shown in **Figure 23**, both top and bottom electrodes were made of steel, which has a negligible resistance (6.9 x 10^{-7} ohm-m at 20°C). Furthermore, the surface of each electrode was attached to a carbon conductive silicon rubber pad. The main functions of the conductive rubber are (a) to give an effective contact between the electrode and the sample as a reasonable pressure was applied and (b) to prevent damage to the electrodes upon measuring electrical resistivity of a rough surfaced sample. The electrical resistivity of the conductive rubber is 0.08-0.12 ohm-m. A spring was attached below the bottom electrode so that the fixture can accommodate various thicknesses of samples and applies sufficient pressure to the sample.

3.2.2 Measurement Schematics

The combination of the high resistance electrometer and the resistivity test fixture enabled the measurement of electrical resistivity, which is an intrinsic property of the material to oppose a charge through a certain volume unit.

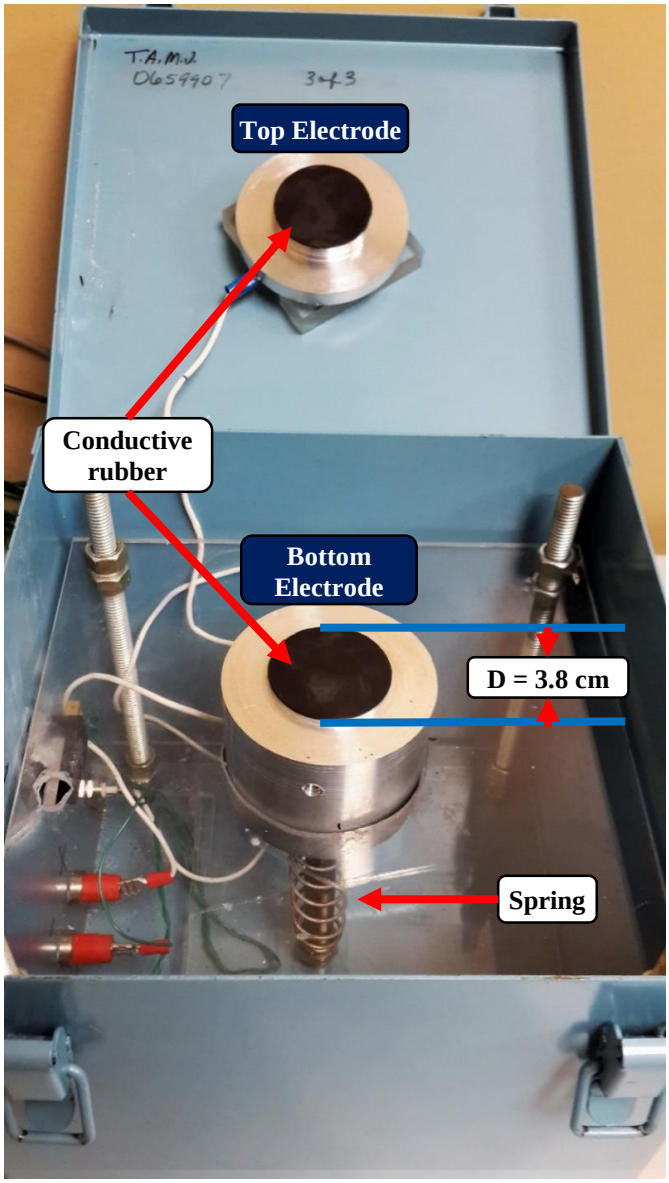

Figure 23: Top and bottom electrodes of the resistivity test fixture.

The measurement of electrical resistivity in this research applied the two-point technique. In this technique, there were three basic processes in measuring the electrical resistivity of the sample. First, the electrometer sourced a known voltage to the sample which was mounted inside the fixture. Second, the electric current that passed through the sample was measured by the electrometer. Lastly, the test voltage and measured current values were used to calculate the electrical resistivity of the sample (subsection 3.2.3). The cable assembly and connection schematic between the electrometer and the resistivity fixture are shown in **Figure 24**.

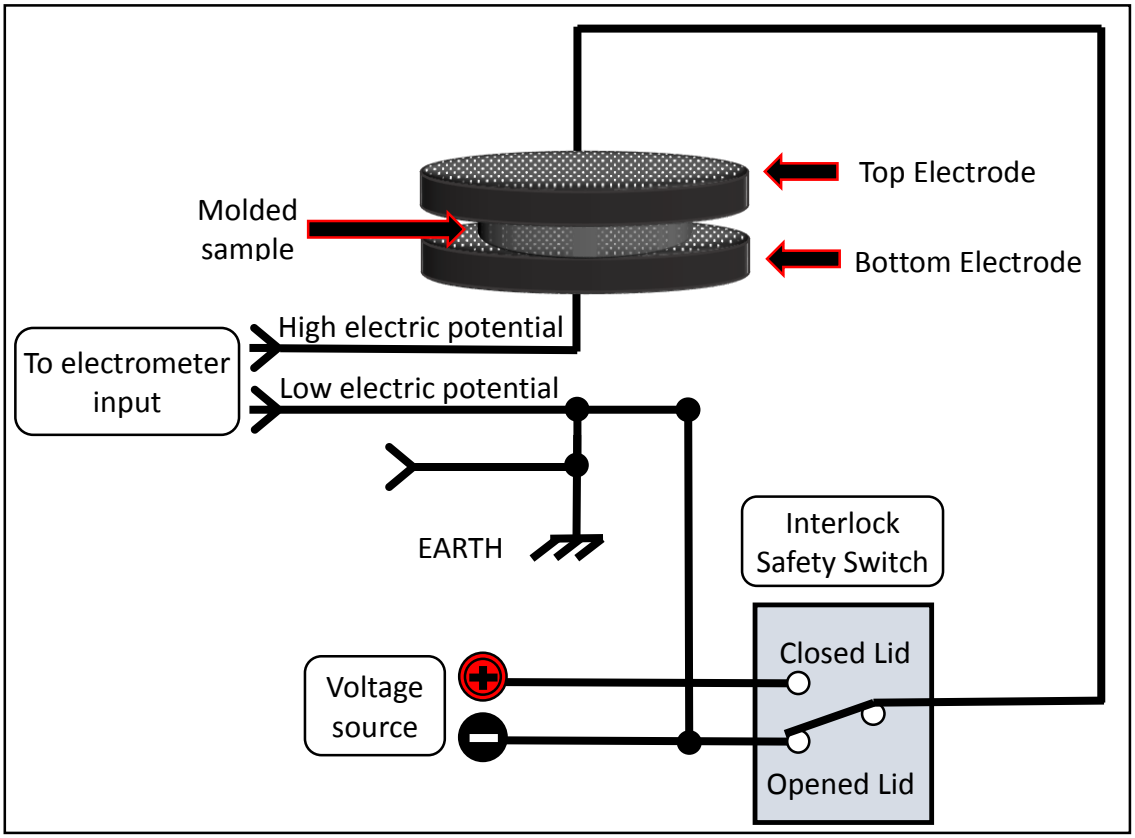

Figure 24: The connection schematic of the high resistance electrometer and the resistivity test fixture.

3.2.3 Electrical Resistivity Calculations

This subsection describes the method to calculate electrical resistivity using the high resistance electrometer and the resistivity test fixture. As mentioned in subsection 3.2.2, the measurement was done by applying a constant voltage on the sample, then the electric current was measured. The electric current (I) between two points in a circuit is proportional to the electric potential difference (ΔV) across it. It is well known as the Ohm's law, which is expressed as

$$\Delta V = IR. \tag{1}$$

The electrical resistance (R) of a material is proportional to its length and inversely proportional to its cross-sectional area. Electrical resistance is given by

$$R = \frac{\rho h}{A}, \tag{2}$$

where h, A, and ρ represent the thickness, cross-sectional area, and the electrical resistivity, respectively. Solving for ρ, we obtain

$$\rho = \frac{A}{h}R. \tag{3}$$

Substituting **Eq. (1)** into **Eq. (3)**, provides

$$\rho = \frac{A}{h}\frac{V}{I}. \tag{4}$$

The cross-sectional area follows the effective area of the sample mounted inside the device. Assuming that the molded disk has an area of a circle, therefore, **Eq. (4)** can be rewritten as

$$\rho = \frac{1/4\,\pi D^2}{h}\frac{V}{I}, \tag{5}$$

where *D* is the effective diameter of the sample. The diameter of the top and bottom electrode of the resistivity fixture is 3.8 cm. The diameter of the sample can be smaller than the electrodes, however, it must be big enough to prevent the top and bottom electrodes to touch each other. The electrical resistivity of each molded sample was calculated based on the input physical dimensions of the test sample.

3.2.4 Electrical Resistivity Measurement Procedure

This research follows certain procedures to make electrical resistivity measurements, as explained below.

1. The first step was safety assessment of the equipment. All cables from the high resistance electrometer and the resistivity test fixture was connected properly to confirm that the equipment worked without any shortages or electric shocks that could cause injury.
2. After turning on the high resistance electrometer, ensure the accuracy of the instrument readings by performing a calibration test.
3. To measure the electrical resistivity, set the measurement type of the equipment to volume resistivity measurement.
4. Clean the surfaces of the top and bottom electrodes using a suitable solvent, such as isopropyl alcohol.
5. Measure the thickness and diameter of the sample using a caliper to obtain an accurate physical dimension of the sample. Next, mount the consolidated disk sample in between the top and bottom electrodes. Avoid handling the sample with

bare fingers by wearing clean non-latex gloves. In mounting the sample, it was important to make sure that there was no gap or conductive paths exist between the electrode and the sample, since it impacted the electrical resistivity reading.

6. Apply 50 V and observe the electrical resistivity value from the front panel of the electrometer. The electrical resistivity gradually changed as the electric current passes through the sample and settles to a certain value after a certain amount of time. The total time when the specified voltage was applied to the sample until the electric current stabilizes is called the electrification time. The electrification time depends on the voltage applied, texture, complexity of the sample, and background offsets and noise around the instrument. A typical electrification time in electrical resistivity measurements is sixty seconds (ASTM Standard D257 - 14 2014).
7. Record the electrical resistivity as soon as the electric current settles and it fluctuates below 1%.

3.3 Numerical Modeling

The measured electrical resistivity values obtained from laboratory experiments of the molded porous kerogen samples are not equal to resistivity of kerogen. Because the effective electrical resistivity measured from the laboratory is influenced by the tortuosity, volumetric concentration, and electrical resistivity of each components (i.e., kerogen particles and pores) in the sample. This thesis uses pore-scale numerical simulation and inversion of electrical resistivity to estimate kerogen resistivity.

The pore-scale numerical simulation was performed on three-dimensional (3D) micro CT scanned images of the molded isolated kerogen sample. Prior to running the numerical simulations, pixel-based segmentations of each image was performed to distinguish the components of the sample. The segmented images were then taken as an input to a previously developed numerical simulator (Chen et al. 2014). The effective electrical resistivity was estimated by numerically solving Laplace's equation, given by

$$\nabla \cdot (\sigma \nabla V) = 0 \tag{6}$$

where σ is the electrical conductivity and V is the electric potential. This equation numerically calculated the electric potential distribution in the sample. The inputs to the numerical simulations include segmented 3D pore-scale images of the porous media, electrical resistivity of the molded components, electric potential difference applied at the boundaries, and the dimensions of the sample. The output of the numerical simulation was the effective electrical resistivity of the sample.

The electrical resistivity of kerogen was estimated by minimizing the difference between the numerically simulated effective electrical resistivity and the laboratory measured electrical resistivity of the molded kerogen samples. With an initial guess of electrical resistivity values of rock components, the numerical simulation was performed to obtain the electric potential distribution and estimate the effective electric resistivity of the sample. The next step was to update the electrical resistivity value of kerogen until the numerically estimated effective electrical resistivity was in good agreement with the one

from laboratory measurements. **Figure 25** is a flowchart that describes the manual inversion method used to estimate the electrical resistivity of the kerogen.

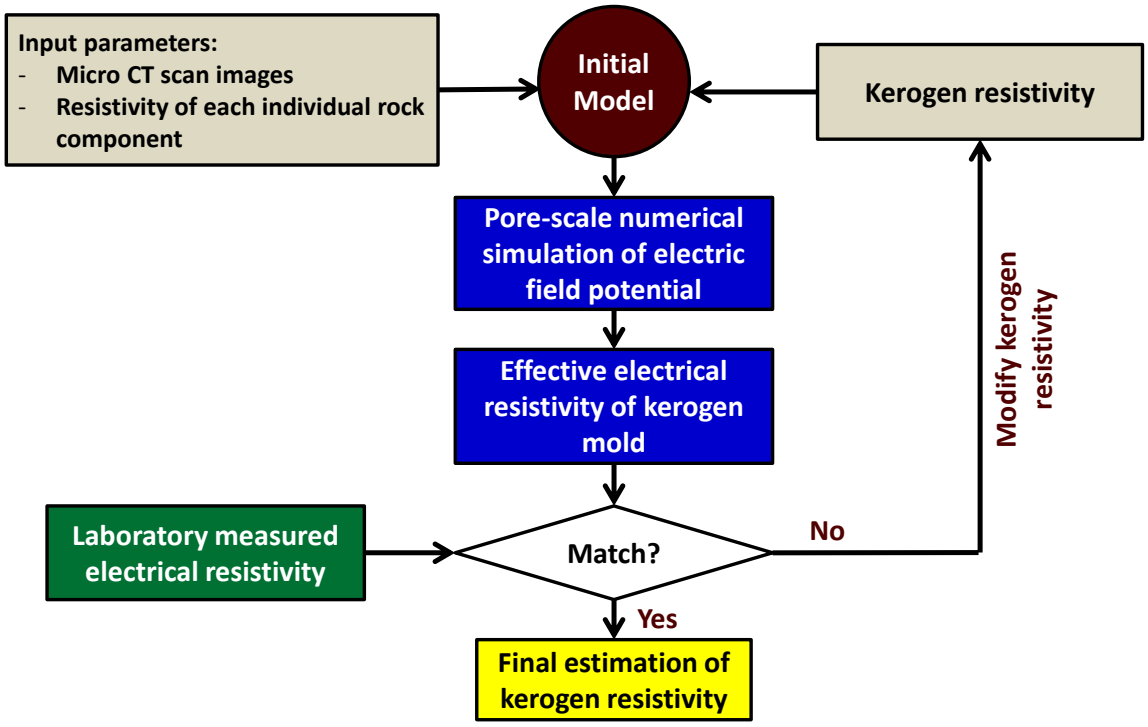

Figure 25: The manual inversion method used to estimate the electrical resistivity of kerogen.

CHAPTER IV

RESULTS

This chapter shows the results obtained from laboratory experiments and numerical simulations. This research uses the Haynesville organic-rich mudrock and the isolated kerogen samples from this formation for a series of laboratory experiments, including synthetic maturation, electrical resistivity measurements, elemental analysis, and Rock-Eval pyrolysis. This chapter also shows how the increasing thermal maturity transforms the chemical structure of the sample and consequently impacts the electrical resistivity measurements. The following subsections provide more details regarding the applied methods.

4.1 Kerogen Isolation and Pyrite Removal Experiment Result

Figure 26 shows the crushed organic-rich mudrock sample and the molded sample from the Haynesville formation. **Figure 27** shows the crushed kerogen sample and its corresponding molded disk.

4.2 XRF Element Maps and Analysis

The experimental work in this research successfully isolated kerogen from the Haynesville mudrock samples. XRF measurements confirmed the significant reduction of carbonates,

silicates, and pyrite in the isolated kerogen samples. **Table 2** summarizes the fluorescence intensity of the elements after each treatment. The pretreatment indicates that the organic-rich mudrock has not been treated with any chemicals. The sample that has been through the first treatment was the isolated kerogen powder that still contains pyrite, which experienced physical and chemical isolation techniques as described in the Chapter II. The second treatment denotes the sample that has been through the pyrite removal treatment. In Table 2, the fluorescence intensity of manganese (Mn) is close to zero, which indicates that manganese had almost no trace in the sample for the pretreatment and first treatment.

(a) (b)

Figure 26: (a) crushed sample and (b) molded samples from Haynesville shale before kerogen isolation.

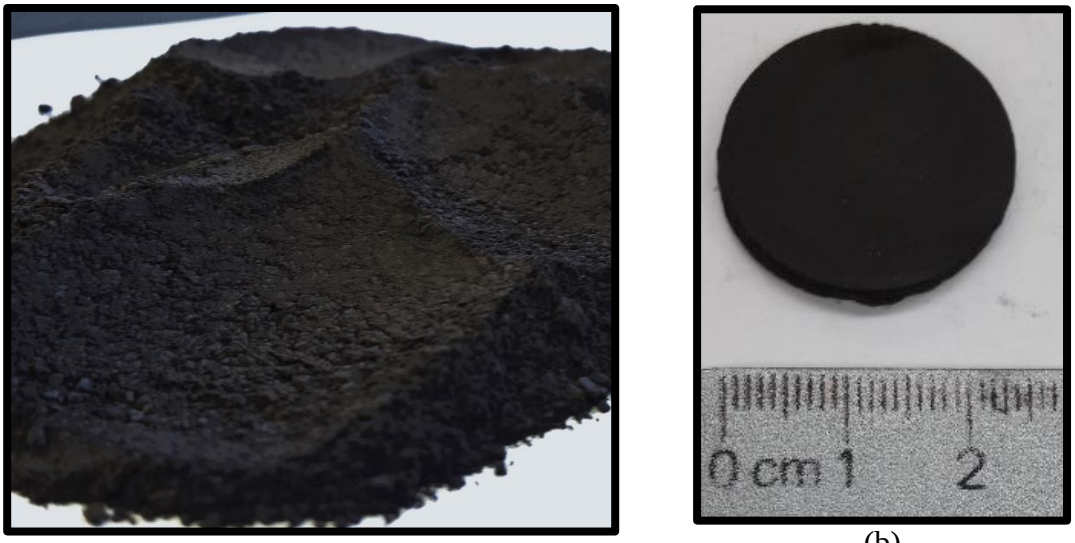

(a) (b)

Figure 27: (a) crushed and (b) molded pyrite-free kerogen samples.

Table 2: The fluorescence intensity of each elements at every step of kerogen isolation procedure: (a) pretreatment, (b) first treatment, and (c) second treatment.

Elements	Pretreatment	First Treatment	Second Treatment
Al	2.274	1.647	0.444
Ca	8.906	1.222	1.005
Fe	14.729	16.97	10.293
K	2.982	6.969	9.907
Mn	0.062	0.046	0.349
S	0.916	4.092	8.593
Si	11.945	8.32	6.115
Ti	0.806	2.399	6.12
Zn	0.433	0.168	0.107

According to Vandenbroucke and Largeau (2007), some minerals were observed to remain as insoluble residues after the kerogen isolation, such as, rutile and anatase (i.e., minerals primarily composed of titanium oxide, TiO_2). Thus the relative quantity of Ti does not change after each treatments. **Table 3** shows the ratio of the mean value of fluorescence

intensity of each elements with respect to Ti (e.g. Ca/Ti). To observe the effect of the kerogen isolation and pyrite removal, the relative difference between the ratios of fluorescence intensity of each elements over Ti (e.g. Ca/Ti) before and after the isolation was calculated (**Table 4**).

Table 3: The ratio of the mean value of fluorescence intensity of each elements over Ti.

Elements	Pretreatment	First Treatment	Second Treatment
Al/Ti	2.82	0.69	0.07
Ca/Ti	11.05	0.51	0.16
Fe/Ti	18.27	7.07	1.68
K/Ti	3.70	2.90	1.62
Mn/Ti	0.08	0.02	0.06
S/Ti	1.14	1.71	1.40
Si/Ti	14.82	3.47	1.00
Zn/Ti	0.54	0.07	0.02

Table 4: The amount of elements changed after first and second treatment, relative to the pretreatment sample. Negative values indicate a decrease of the element, conversely, positive values indicate an increased quantity in the sample.

Elements	% Change after 1st Treatment	% Change after 2nd Treatment
Al	-76%	-97%
Ca	-95%	-99%
Fe	-61%	-91%
K	-21%	-56%
Mn	-75%	-26%
S	50%	24%
Si	-77%	-93%
Zn	-87%	-97%

The result shows that the amount of calcium (Ca), potassium (K), and silica (Si) has been substantially decreased for the isolated kerogen samples. It indicated that the kerogen isolation technique successfully dissolved a significant amount of carbonates, silicates, feldspar, and clays. Furthermore, the pyrite removal was successful as the iron (Fe) was

depleted by 91%. The increased amount of sulfur (S) indicated that there was a relative increase of organic sulfur in the sample as the kerogen was more concentrated.

4.3 Rock-Eval Pyrolysis Analysis

The influence of synthetic maturation by heat-treatment and kerogen isolation on geochemical parameters was evaluated by the Rock-Eval pyrolysis result. **Table 5** summarizes the geochemical parameters obtained from the Rock-Eval pyrolysis. The impact of the kerogen isolation procedure on geochemical parameters was obvious in the difference in TOC between the mudrock and the isolated kerogen samples. The Rock-Eval pyrolysis data showed that the TOC in the isolated kerogen can be 10 fold higher (wt%) to that of the mudrock. There was also a noticeable difference in T_{max} and HI between the mudrock and isolated kerogen samples. The T_{max} of mudrock samples was as 100°C higher than the isolated kerogen samples. Similarly, HI was also affected as the values dropped after the kerogen isolation. Similarly, HI was also affected as the values dropped after the kerogen isolation.

The impact of synthetic maturation of both powdered mudrock and isolated kerogen samples on geochemical parameters was observed from the variation of Tmax and HI values, as shown in **Figure 28 and 29**, respectively. In general, as the heat-treatment temperature increases, the T_{max} increases and the HI decreases. However, the T_{max} for

mudrock and isolated kerogen samples at 800°C did not follow the increasing trend. These samples had S2 values lower than 0.5 mg HC/g, which led to an inaccurate determination of T_{max}, and consequently, an inaccurate indication of thermal maturity. Thus, the HI values were used to validate the thermal maturity. The Rock-Eval pyrolysis data showed that the HI of all samples depleted as the heat-treatment temperature increased (Figure 29). During synthetic maturation, the unheated rock samples that contain abundant aliphatic components evolved to form aromatic ring structures. This led to a decrease in the relative concentration of aliphatic carbon in the kerogen structure and consequently reduce the corresponding HI in the sample.

Table 5: Rock-Eval Pyrolysis Results for the Samples from the Haynesville Formation.

Sample	Heat-Treatment Temperature (°C)	TOC (wt%)	S1 ($^{mg}/_{g}$)	S2 ($^{mg}/_{g}$)	S3 ($^{mg}/_{g}$)	T_{max} (°C)	HI ($^{S2x100}/_{TOC}$)	OI ($^{S3x100}/_{TOC}$)
Mudrock Sample	25	4.83	0.2	0.86	0.38	514	18	8
	150	4.55	0.18	0.76	0.46	517	17	10
	300	4.3	0.13	0.57	0.45	516	13	10
	425	4.63	0.13	0.58	0.47	531	13	10
	500	4.61	0.12	0.32	0.5	592	7	11
	650	4.48	0.12	0.13	0.57	607	3	13
	800	3.93	0.11	0.09	0.69	408	2	18
Isolated Kerogen Sample	25	39.48	2.92	16.01	2.72	408	41	7
	150	30.92	1.42	10.42	1.95	407	34	6
	300	29.94	0.59	7.84	3.03	410	26	10
	425	27.32	0.12	0.18	0.79	459	1	3
	500	24.1	0.16	0.13	0.72	475	1	3
	650	28.7	0.69	0.22	4.99	606	1	17
	800	38.59	1.04	1.1	12.51	411	3	32

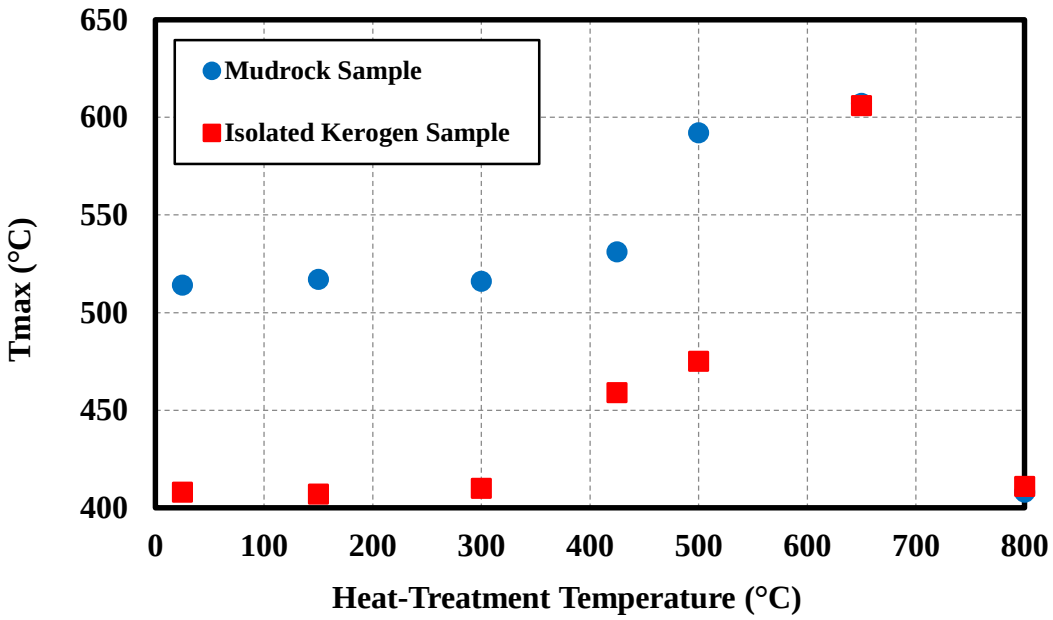

Figure 28: The impact of heat-treatment temperature on the T_{max} of powdered mudrock and isolated kerogen samples.

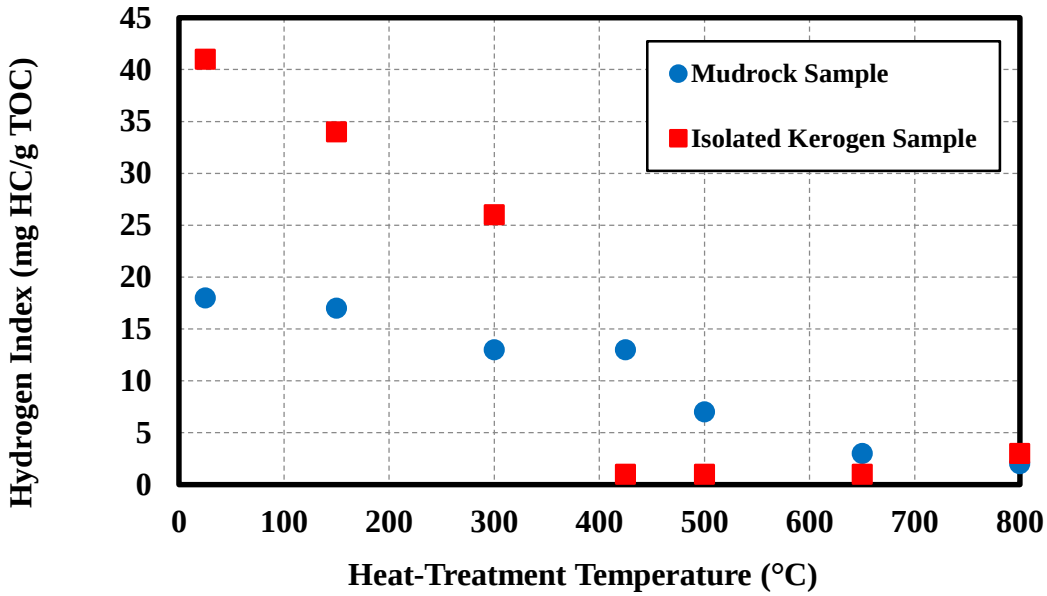

Figure 29: The impact of heat-treatment temperature on the HI of powdered mudrock and isolated kerogen sample.

4.4 The Effect of Thermal Maturity on Electrical Resistivity

This section shows the effect of the synthetic maturation on the measured electrical resistivity of organic-rich mudrock and molded kerogen samples. **Figure 30** shows the relationship between thermal maturity and electrical resistivity of the Haynesville rock samples. The electrical resistivity of all samples were measured at room temperature (25 ± 2°C).

The electrical resistivity of the mudrock sample (blue) increased three order of magnitudes from $2.4x10^5$ ohm-m to $2.4x10^8$ ohm-m as the heat-treatment temperature was increased from 25°C (room temperature) to 300°C. Above 300°C, the electrical resistivity declined

as much as four orders of magnitude until the heat-treatment temperature of the sample reached 800°C. The electrical resistivity of the molded kerogen sample (red) was 1 order of magnitude lower than the mudrock sample. The measured electrical resistivity followed the same trend with the mudrock sample, which increased three order of magnitudes until 300°C, and dropped to $1.79x10^3$ ohm-m when heat-treatment temperature was 800°C.

The increase of electrical resistivity as the heat-treatment temperatures were increased from room temperature to 300°C was attributed to the loss of free moisture and water molecules that were embedded within the mudrock and kerogen molded samples. The electrical resistivity measured on all samples decreased exponentially for those that have been heat-treated from 300°C to 800°C. This drop was attributed to the increasing carbon content as a result of thermal decomposition of the kerogen (Duba 1977; Rajeshwar 1979; Duba 1983). The increased quantity of the total carbon was in fact a process of graphitization that occurred with increasing thermal maturity (Walters et al. 2014). As the heat treatment temperature increased, the volatile components gradually diminish and the increasing amount of graphite-like material in the sample ultimately created a connection with each other and able to conduct electric current (Celzard et al. 1999). Another reason for this decrease in electrical resistivity can be the increase in aromaticity of the samples during maturation. The change in aromaticity as a function of maturity requires further investigation.

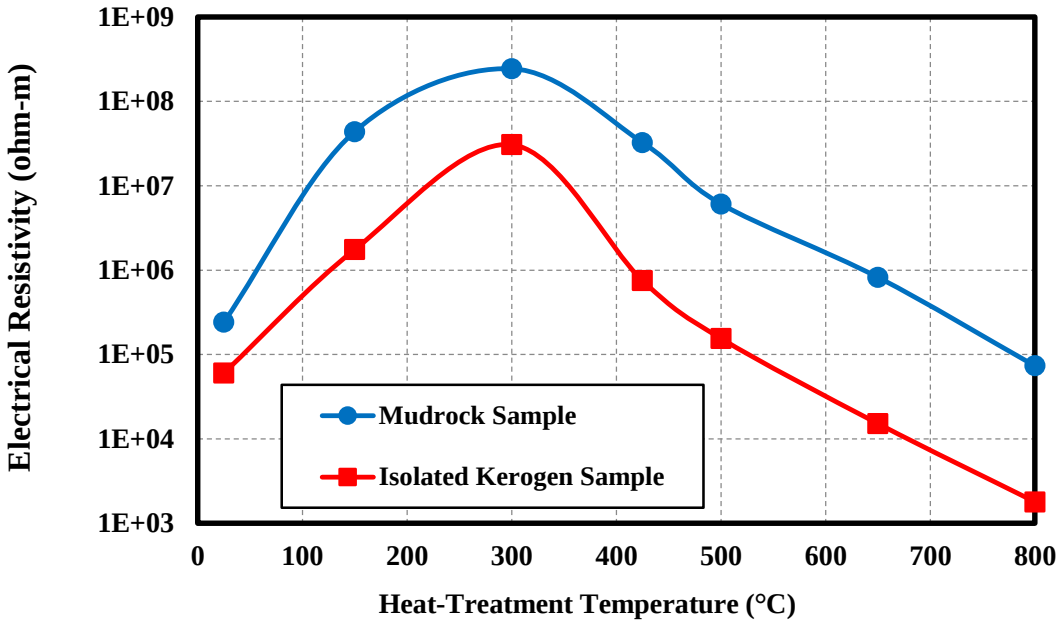

Figure 30: The effect of heat-treatment temperature of mudrock and isolated kerogen on electrical resistivity of the samples.

The electrical resistivity measurements in this thesis were performed at room temperature. It is important to note that the electrical resistivity values measured for pure kerogen will be less than what reported if measured at reservoir temperature.

4.5 TEM Imaging

The appearance of graphite-like materials in kerogen structure under heat-treatment was studied using TEM imaging. **Figure 31** shows a TEM image of the unheated mudrock with amorphous structure (yellow box). Based on the elemental analysis, alumina silicate

crystalline structures were detected (green box) in the image. The presence of graphite-like materials cannot be observed in this case.

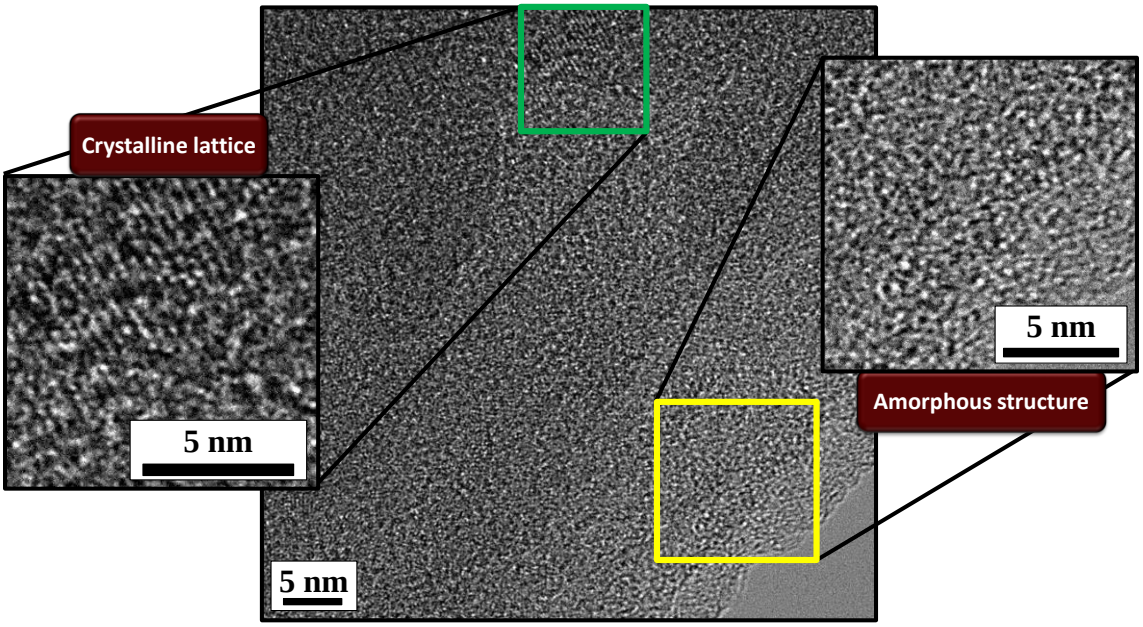

Figure 31: TEM image of unheated mudrock sample from the Haynesville formation.

Figure 32 shows the TEM image of the synthetically matured isolated kerogen sample (heat-treated up to 800°C), which depicts a certain area that contains amorphous carbon (blue box). In this region, continuous long fringes were not observed, however, short-range layers (3nm) were still observable (white arrow). These short and discontinuous structures are called basic structural units (BSU), which contain several aromatic rings (Oberlin et al. 1980). In the red box region, graphitization of the organic matter occurred as the graphite-like materials were forming to layered sheets. The presence of graphite-like sheets alongside the amorphous carbon material shows that the isolated kerogen sample was in the process of graphitizing.

The presence of graphite-like sheets in samples with higher maturity impacted electrical resistivity measurements. The TEM images shown in this thesis indicated that graphitization occurred in thermally mature samples. Discontinued graphite-like fringes appeared in layers for the matured isolated kerogen samples. The presence of long structured and layered graphite sheets were not observed because (a) the sample was cut to 80 nm which may disrupt the graphite-like network and (b) TEM only produce two-dimensional (2D) images, not allowing the 3D connection of the fringes to be observed (Walters et al. 2014).

4.6 Numerical Simulation Result

The input to numerical simulations was 3D pore-scale images of molded kerogen obtained from micro CT scan images, as shown in **Figure 33**. The volumetric concentration of pyrite and kerogen in the molded kerogen sample was 1% and 81%, respectively. The porosity of the molded kerogen was 18%. Electrical resistivity of pores was assumed to be 10^7 ohm-m. The initial guess of resistivity for kerogen was 50 ohm-m. The kerogen resistivity was updated until the simulated resistivity of the kerogen mold converged to the measured value.

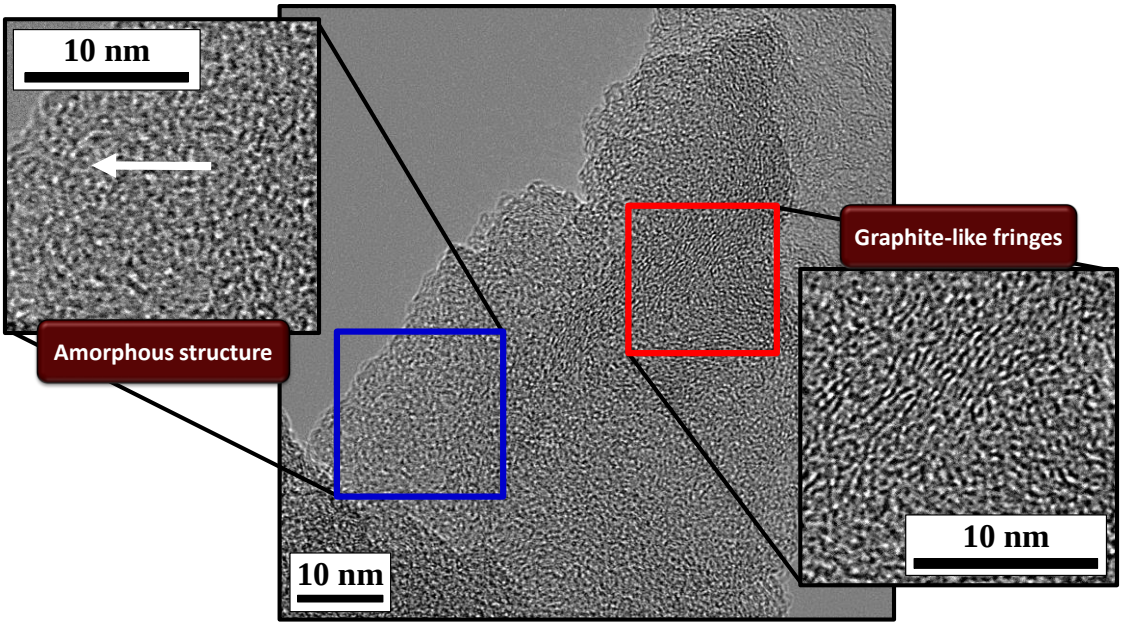

Figure 32: TEM image of synthetically matured isolated kerogen sample from the Haynesville formation (heat-treated up to 800°C).

Figure 34 shows the estimated electrical resistivity of kerogen extracted from the Haynesville rock samples. The estimated resistivity values were obtained from the measured electrical resistivity of the molded samples after applying corrections for the pore network of the molded samples through numerical simulations.

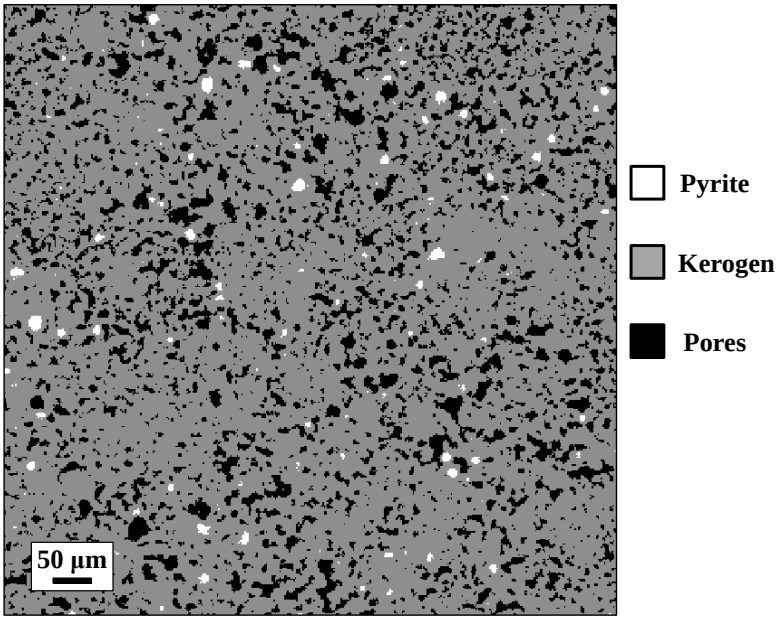

Figure 33: 2D Micro CT scan image of the molded kerogen. The pyrite, kerogen, and pores are depicted in white, grey, and black color, respectively.

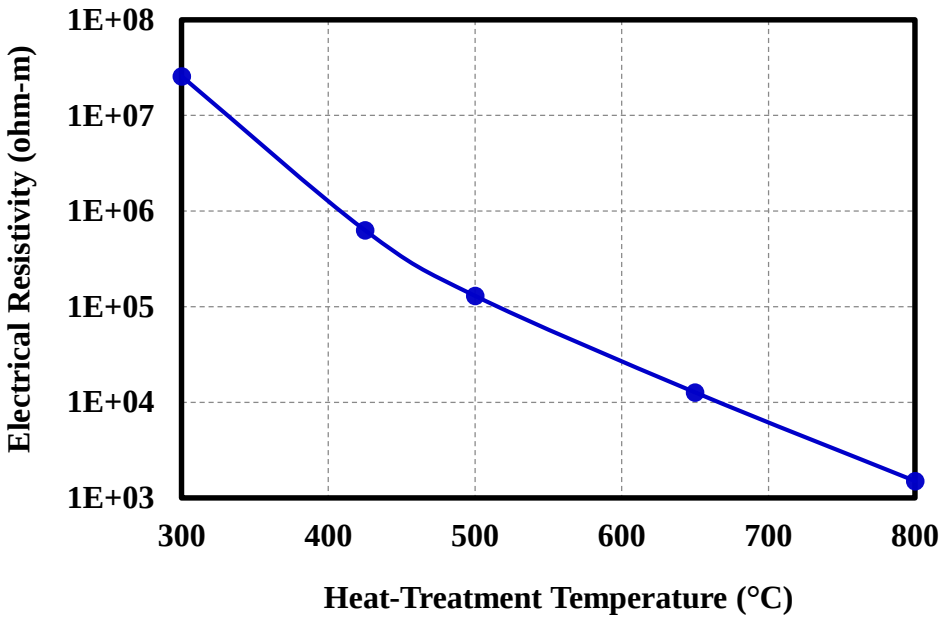

Figure 34: The estimated electrical resistivity of the isolated kerogen from the Haynesville rock samples, obtained from the measured electrical resistivity of the molded samples after applying corrections for the pore network of the molded samples through numerical simulations.

CHAPTER V

SUMMARY AND CONCLUSIONS

This chapter is a summary of the work and result obtained in this thesis. It also presents the conclusions and recommendations for future work.

5.1 Summary

This thesis for the first time quantifies the electrical resistivity of kerogen and organic-rich mudrock samples as a function of thermal maturation in the Haynesville shale. The electrical resistivity measurements were performed at room temperature. First, this research employed a kerogen isolation technique using the combination of physical and chemical methods. To remove pyrite from the kerogen sample, this research performed pyrite removal experiment using acidic $CrCl_2$ solution in a nitrogen chamber. The result of these techniques was the isolated pyrite-free kerogen powder.

All of the investigated samples were synthetically matured to different degrees of maturation by heat-treatment in a vacuum up to 800°C. The geochemical analysis was performed on the heat-treated mudrock sample and the pyrite-free kerogen powder using XRF and Rock-Eval pyrolysis. XRF measurements recorded the decreasing amount of carbonates, silicates, clays, and pyrite from the rock samples after each isolation treatment. The Rock-Eval pyrolysis result showed the impact of synthetic maturation on geochemical

properties of mudrock and isolated kerogen samples, such as T_{max} and HI. The heat-treatment temperature, T_{max}, and HI were the parameters that indicated the thermal maturity parameter in this research.

The next step was to prepare the isolated kerogen samples for electrical resistivity measurements. A specifically designed mold frame was used to compress the kerogen powder to form a solid, smooth-surfaced disk. The electrical resistivity of the mudrock and the molded kerogen sample was measured was using a high resistance electrometer coupled with a newly designed resistivity test fixture. This research investigated the impact of thermal maturity on the electrical resistivity of each samples. The electrical resistivity of the mudrock and molded kerogen samples increased up to three order of magnitudes when synthetically matured using heat-treatment from 25°C to 300°C. When the heat-treatment temperature was increased from 300°C to 800°C, the electrical resistivity decreased up to four orders of magnitude for both, mudrock and the molded kerogen samples. The electrical resistivity of the molded kerogen sample was 1 order of magnitude lower than the mudrock sample.

Finally, this research investigated the impact of maturation on the formation of graphite-like structures in the powdered mudrock and isolated kerogen samples using TEM imaging. In the case of the unheated mudrock sample, crystalline structures of clay and amorphous carbon structure were detected. In the case of the synthetically matured

isolated kerogen sample, the TEM image showed that graphitization of the organic matter occurred as the graphite-like materials are forming to layered sheets.

5.2 Conclusions

This research involved a series of laboratory experiments to investigate the impact of thermal maturity on electrical resistivity of mudrock and isolated kerogen samples. The conclusions that can be drawn from this research are as follows:

1. The proposed combinations of physical isolation technique, chemical demineralization, and pyrite removal served as a benchmark to extract pure isolated kerogen from organic-rich mudrocks.
2. Kerogen isolation enabled direct physical measurements on pure kerogen samples, including geochemical analysis (i.e., XRF and Rock-Eval pyrolysis) and electrical resistivity.
3. XRF measurements confirmed the absence of carbonates, silicates, clays, and pyrite in the isolated kerogen samples.
4. The relationship between thermal maturity and electrical resistivity of organic-rich mudrock and kerogen samples indicated that chemical structure transformation occurs upon synthetic maturation.
5. The electrical resistivity increased up to three orders of magnitude when the samples were heat-treated from 25°C to 300°C. This is attributed to the loss of free

moisture and water molecules that were embedded within the mudrock and kerogen samples.

6. In contrast, the electrical resistivity decreased up to four orders of magnitude when the samples were heat-treated from 300°C to 800°C. This can be attributed to the increase in concentration of graphite-like materials in the samples, which was shown by TEM image of the synthetically matured isolated kerogen sample.
7. The electrical resistivity measurements in this thesis were performed at room temperature (25 ± 2°C). The electrical resistivity values measured for pure kerogen will be less than what reported if measured at reservoir temperature.
8. The outcome of this research can potentially improve the interpretation of electrical resistivity logs in organic-rich mudrocks, which can lead to enhanced well-log-based assessment of in situ hydrocarbon saturation.

5.3 Recommendations for Future Work

Further measurements are needed to investigate the characteristics of kerogen and how it impacts the interpretation of petrophysical properties in organic-rich mudrocks. The areas of further research that could contribute to this thesis include:

- The measurements of electrical resistivity using alternating current (AC) will undoubtedly contribute to a better understanding of electrical properties of kerogen, measured by borehole geophysical measurements.

- Further measurements are needed to investigate the electrical resistivity of isolated kerogen at higher heat-treatment temperatures, ranging from 1000°C to 3000°C. Within this temperature window, it is necessary to perform a nano-scale observation of the structural transformation and investigate its corresponding geochemical properties.
- Quantitative assessment of the impact of aromaticity on the electrical resistivity of organic-rich mudrock and isolated kerogen samples.
- A comprehensive study on the impact of different types and maturity levels of organic-rich mudrocks from various formations on electrical resistivity.
- Extensive investigation and quantification of the impact of kerogen on electrical resistivity of the rock and the estimates of hydrocarbon saturation.

REFERENCES

Aboulkas, A. and El-Harfi, K. 2009. Effects of Acid Treatments on Moroccan Tarfaya Oil Shale and Pyrolysis of Oil Shale and their Kerogen. *Journal of Fuel Chemistry and Technology* **37** (6): 659–667.

Acholla, F.V. and Orr, W.L. 1993. Pyrite Removal from Kerogen without Altering Organic Matter: The Chromous Chloride Method. *Energy and Fuels* **7**: 406-410.

Archie, G.E. 1942. The Electrical Resistivity Log as an Aid in Determining Some Reservoir Characteristics. *Transactions of the American Institute of Mining, Meterology, and Petroleum Engineering* **146** (1): 54–62.

Al-Harahsheh, A.M., Al-Harahsheh, M., Al-Otoom, A., and Allawzi, M. 2009. Effect of Demineralization of El-lajjun Jordanian Oil Shale on Oil Yield. *Fuel Processing Technology* **90**: 818–824.

ASTM Standard D257 - 14, 2014, "Standard Test Methods for DC Resistance or Conductance of Insulating Materials," ASTM International, West Conshohocken, PA, 2014.

Ballice, L. 2006. Stepwise Chemical Demineralization of Goynuk (Turkey) Oil Shale and Pyrolysis of Demineralization Products. *Industrial & Engineering Chemistry Research* **45**: 906-912.

Ballice, L. 2004. Effect of Demineralization on Yield and Composition of the Volatile Products Evolved from Temperature-Programmed Pyrolysis of Beypazari (Turkey) Oil Shale. *Fuel Processing Technology* **86**: 673– 690.

Buseck, P.R. and Beyssac, O. 2014. From Organic Matter to Graphite: Graphitization. *Elements* **10**: 421-426.

Canfield, D.E., Raiswell, R., Westrich, J.T., Reaves, C.M., and Berner, R.A. 1986. The Use of Chromium Reduction in the Analysis of Reduced Inorganic Sulfur in Sediments and Shales. *Chemical Geolology* **54**: 149-155.

Celzard, A., Mareche, J.F., Payot, F., Bégin, D., and Furdin, G. 2000. Electrical Conductivity of Anthracites as a Function of Heat Treatment Temperature. *Carbon* **38**: 1207-1215.

Chen, H., Firdaus, G., and Heidari, Z. 2014. Impact of Anisotropic Nature of Organic-Rich Source Rocks on Electrical Resistivity Measurements. Presented at the

SPWLA 55th Annual Logging Symposium, Abu Dhabi, United Arab Emirates, 18-22 May.

Chen, H., Chi, L., Kethireddy, N., and Hediari, Z. 2013. Impact of Spatial Distribution of Kerogen Network on Electrical Resistivity of Organic-Rich Source Rocks. Paper SPE 168923 presented at the Unconventional Resources Technology Conference, Denver, Colorado, USA, 12-14 August.

Clavier, C., Coates, G., and Dumanoir, J. 1984. Theoretical and Experimental Bases for the Dual-Water Model for Interpretation of Shaly Sands. *Society of Petroleum Engineers Journal* **24** (2): 153–168.

Clennell, M.B., Josh, M., Esteban, L., Piane, C.D., Schmid, S., Verrall, M., Hill, D., Woods, C., and McMullan, B. 2010. The Influence of Pyrite on Rock Electrical Properties: A Case Study from NW Australian Gas Reservoirs. Paper SPWLA 97081 presented at the SPWLA 51st Annual Logging Symposium, Perth, Australia, 19-23 June.

Curtis, M.E., Sondergeld, C.H., Ambrose, R.J., and Rai, C.S. 2012. Microstructural Investigation of Gas Shales in Two- and Three Dimensions Using Nanometer-Scale Resolution Imaging. *American Association of Petroleum Geologists Bulletin* **96**: 665-677.

Curtis, M.E., Ambrose, R. J., Sondergeld, C.H., and Rai, C.S. 2011. Transmission and Scanning Electron Microscopy Investigation of Pore Connectivity of Gas Shales on the Nanoscale. Paper SPE 144391 presented at the North American Unconventional Gas Conference and Exhibition, Woodlands, Texas, USA, 14-16 June.

Daniels, H., Brydson, R., Rand, B., and Brown, A. 2007. Investigating Carbonization and Graphitization Using Electron Energy Loss Spectroscopy (EELS) in the Transmission Electron Microscope (TEM). Philosophical Magazine 87 (27): 4073-4092.

Dellisanti, F., Pini, G.A., and Baudin, F. 2010. Use of T_{max} as a Thermal Maturity Indicator in Orogenic Successions and Comparison with Clay Mineral Evolution. *Clay Minerals* **45**: 115–130.

Duba, A.G. 1983. Electrical Conductivity of Colorado Oil Shale to 900°C. *Fue*l **62**: 966-972.

Duba, A.G. 1977. Electrical Conductivity of Coal and Coal Char. *Fuel* **56**: 441-443

Durand, B. 1980. Sedimentary Organic Matter and Kerogen. Definition and Quantitative Importance of Kerogen. In *Kerogen: Insoluble Organic Matter from Sedimentary Rocks*, ed. B. Durand, Chap. 1, 13-34. Paris: Éditions Technip.

Durand, B. and Nicaise G. 1980. Procedure of Kerogen Isolation. In *Kerogen: Insoluble Organic Matter from Sedimentary Rocks*, ed. B. Durand, Chap. 2, 35-52. Paris: Éditions Technip.

Forsman, J.P. 1963. *Geochemistry of Kerogen*. Chap. 5, 148–182. Tulsa, Oklahoma: Jersey Production Research Company.

Forsman, J.P. and Hunt, J.M. 1958. Insoluble Organic Matter (Kerogen) in Sedimentary Rocks of Marine Origin. *Geochimica et Cosmochimica Acta* **15**: 170-182.

Goklen, K.E., Stoecker, T.J., and Baddour, R.F. 1984. A Method for the Isolation of Kerogen from Green River Oil Shale. *Industrial & Engineering Chemistry Product Research and Development* **23** (2): 308-311.

Harrison, W.E. 1979. Levels of Graphitization of Kerogen as a Potentially Useful Method of Assessing Paleotemperatures. *The Society of Economic Paleontologists and Mineralogists (SEPM)* **26**: 45-53.

Harwood, R.J. 1977. Oil and Gas Generation by Laboratory Pyrolysis of Kerogen. *AAPG Bulletin* **61**: 2082-2102.

Hubbard, A.B., Smith, H.N., Heady H.H., and Robinson, W.E. 1952. Method of Concentrating Kerogen in Colorado Oil Shale by Treatment with Acetic Acid and Gravity Separation. Washington, D.C.: United States. Dept. of the Interior, Bureau of Mines.

Katz, B.J. 1983. Limitations of 'Rock-Eval' Pyrolysis for Typing Organic Matter. *Organic Geochemistry* **4** (3): 195-199.

Kennedy, M.C. 2004. Gold Fool's: Detecting, Quantifying and Accounting for the Effects of Pyrite on Modern Logs. Paper presented at the SPWLA 45th Annual Logging Symposium, Noordwijk, Netherlands, 6-9 June.

Kethireddy, N., Chen, H., and Heidari, Z. 2014. Quantifying the Effect of Kerogen on Resistivity Measurement in Organic-Rich Mudrocks. *Petrophysics* **55** (2): 136-146.

Lamey, S.C. and Childers, E.E. 1977. Organic Composition of Devonian Shale from Perry County, Kentucky. Report MERC/TPR-77/3, United States Department of Energy

Morgantown Energy Research Center, Morgantown, West Virginia (December 1977).

Lis, G. P., Mastalerz, M., and Schimmelmann, A. 2008. Increasing Maturity of Kerogen Type II Reflected by Alkylbenzene Distribution from Pyrolysis-Gas Chromatography–Mass Spectrometry. *Organic Geochemistry* **39** (4): 440–449.

Love, A.H. 1982. Kerogen-Isolation Method—A Study with Kerogen Data from Sedimentary Rocks. Report No. 82-981. United States Department of the Interior Geological Survey.

McIver, R.D. 1962. Ultrasonics – A Rapid Method for Removing Soluble Organic Matter from Sediments. *Geochemica et Cosmochimica Acta* **26**: 343-345.

Meng, D., Ma, T., Geng, C., and Sun, Y. 2012. Test Method and Experimental Research on Resistance of Oil Shale under High Temperature. *Global Geology* **15** (3): 245–251.

Milner, M., McLin, R., and Petriello, J. 2010. Imaging Texture and Porosity in Mudstones and Shales: Comparison of Secondary and Ion-Milled Backscatter SEM Methods. Paper CSUG/SPE 138975 presented at the Canadian Unconventional Resources and International Petroleum Conference, Calgary, Alberta, Canada, 19-21 October.

Nordeng, S.H. 2012. Basic Geochemical Evaluation of Unconventional Resource Plays. *Geo News* **39** (1): 14-18.

Passey, Q.R., Bohacs, K.M., Esch, W.L., Klimentidis, R., and Sinha, S. 2010. From Oil-Prone Source Rock to Gas-Producing Shale Reservoir – Geologic and Petrophysical Characterization of Unconventional Shale-Gas Reservoirs. Paper SPE 131350 presented at the CPS/SPE International Oil and Gas Conference and Exhibition, Beijing, China, 8–10 June.

Passey, Q.R., Creaney, S., Kulla, J.B., Moretti, F.J., and Stroud, J.D. 1990. A Practical Model for Organic Richness from Porosity and Resistivity Logs. *The American Association of Petroleum Geologists Bulletin* **74** (12): 1777-1794.

Peters, K.E. 1986. Guidelines for Evaluating Petroleum Source Rock Using Programmed Pyrolysis. *The American Association of Petroleum Geologists Bulletin* **70** (3): 318-329.

Quass, F.W. 1939. The Analysis of the Kerogen of Oil Shales. *Journal of the Institute of Petroleum* 25: 813-819.

Rajeshwar, K., Das, M., and DuBow, J. 1980. D.C. Electrical Conductivity of Green River Oil Shales. *Nature* **287**: 131-133.

Rajeshwar, K., Nottenburg, R., and Dubow, J. 1979. Review Thermophysical Properties of Oil Shales. *Journal of Materials Science* **14**: 2025-2052.

Reaves, C. M. 1984. The Migration of Iron and Sulfur during the Early Diagenesis of Marine Sediments. PhD dissertation, Yale University, New Haven, Connecticut (December 1984).

Robinson, W.E. 1969. Isolation Procedures for Kerogens and Associated Soluble Organic Materials. In *Organic Geochemistry*, ed. G. Eglinton and M.T.J. Murphy, Chap. 6, 181–195. New York: Springer-Verlag, Berlin Heidelberg.

Robl, T.L. and Davis, B.H. 1993. Comparison of the HF-HCl and HF-BF_3 Maceration Techniques and the Chemistry of Resultant Organic Concentrates. *Organic Geochemistry* **20** (2): 249–255.

Rojas, K.M.K.K., Niemann, M., Palmowski, D., Peters, K., and Stankiewicz, A. 2011. Basic Petroleum Geochemistry for Source Rock Evaluation. *Oilfield Review* **23** (2): 32-43.

Saidian, M., Kuila, U., Rivera, S., Godinez, L. J., and Prasad, M. 2014. Porosity and Pore Size Distribution in Mudrocks: A Comparative Study for Haynesville, Niobrara, Monterey and Eastern European Silurian Formations. Paper SPE 1922745 presented at the Unconventional Resources Technology Conference, Denver, Colorado, USA, 25-27 August.

Saxby, J.D. 1970. Isolation of Kerogen in Sediments by Chemical Methods. *Chemical Geology* **6**: 173-184.

Schmoker, J.W. and Hester, T.C. 1990. Formation Resistivity as an Indicator of Oil Generation – Bakken Formation of North Dakota and Woodford Shale of Oklahoma. *The Log Analyst* 31 (1): 1-9.

Shabro, V., Kelly, S., Torres-Verdin, C., Sepehrnoori, K., Revil, A. 2014. Pore-scale Modeling of Electrical Resistivity and Permeability in FIB-SEM Images of Organic Mudrock. *Geophysics* **79**: 289-299.

Shabro, V., Torres-Verdin, C., and Javadpour, F. 2011. Pore-scale Quantification of Apparent Permeability and Electrical Resistivity of Hydrocarbon-Bearing Shale in the Presence of Gas Desorption. Paper SPWLA-2011-K presented at the SPWLA 52nd Annual Logging Symposium, Colorado Springs, Colorado, USA, 14-18 May.

Sisk, C., Diaz, E., Walls, J., Grader, A., and Suhrer, M. 2010. 3D Visualization and Classification of Pore Structure and Pore Filling in Gas Shales. Paper SPE 134582 presented at the SPE Annual Technical Conference and Exhibition, Florence, Italy, 19-22 September.

Smith, J.W. 1961. Ultimate Composition of Organic Material in Green River Oil Shale. Report 5725, USDOI, United States Bureau of Mines, Washington, D.C.

Smith, M.W., Shadle, L.J., and Hill, D.L. 2007. Oil Shale Development from the Perspective of NETL's Unconventional Oil Resource Repository. Presented at the 26th Oil Shale Symposium, Golden, Colorado, 16-20 October.

Sondergeld, C.H., Rai, C.S., and Curtis, M.E. 2013. Relationship between Organic Shale Microstructure and Hydrocarbon Generation. Paper SPE 164540 presented at the SPE Unconventional Resources Conference-USA, The Woodlands, Texas, USA, 10-12 April.

Sondergeld, C.H., Ambrose, R.J., Rai, C.S., and Moncrieff, J. 2010. Micro-Structural Studies of Gas Shales. Paper SPE 131771 presented at the SPE Unconventional Gas Conference, Pittsburgh, Pennsylvania, USA, 23-25 February.

Song W. N., Dong, Y. L., Xue, L. M., Ding, H. X., Li, Z., and Zhou, G. J. 2012. Hydrofluoric Acid-Based Ultrasonic Upgrading of Oil Shale and Its Structure Characterization. *Oil Shale* **29** (4): 334–343.

Spiro, B. 1991. Effects of Minerals on Rock Eval Pyrolysis of Kerogen. *Journal of Thermal Analysis* **37**: 1513-1522.

Tamimi, A. and Uysal, B.Z. 1990. Parametric Investigation of Oil Shale Extraction with Organic Solvents. *Chemie Ingenieur Technik* **62** (10): 847-849.

Torrente, M.C. and Galan, M.A. 2011. Extraction of Kerogen from Oil Shale (Puertollano, Spain) with Supercritical Toluene and Methanol Mixtures. *Industrial & Engineering Chemistry Research* **50**: 1730–1738.

Tuttle, M.L., Goldhaber, M.B., and Williamson, D.L. 1986. An Analytical Scheme for Determining Forms of Sulphur in Oil Shales and Associated Rocks. *Talanta* **12**: 953-961.

Vandenbroucke, M. 2003. Kerogen: from Types to Models of Chemical Structure. *Oil & Gas Science and Technology – Rev. IFP* **58** (2): 243-269.

Vandenbroucke, M. and C. Largeau, C. 2007. Kerogen Origin, Evolution and Structure. *Organic Geochemistry* **38** (5): 719–833.

Walters, C.C., Kliewer, C.E., Awwiller, D.N., Rudnicki, M.D., Passey, Q.R., and Lin, M.W. 2014. Influence of Turbostratic Carbon Nanostructures on Electrical Conductivity in Shales. *International Journal of Coal Geology* **122**: 105–109.

Wang, C., Yao, J., Wu, K., Ren, G., Sun, H., Yang, Y., Gao, Y., and Chen, Z. 2014. Organic and Inorganic Pore Structure Analysis in Shale Matrix with Superposition Method. Paper SPE 1922283 presented at the Unconventional Resources Technology Conference, Denver, Colorado, USA, 25-27 August.

Waxman, M.H. and Smits, L.J.M. 1968. Electrical Conductivities in Oil-Bearing Shaly Sands. *Society of Petroleum Engineers Journal* **8**: 107-122.

Zhao, P., Zhao, Y., Zou, C., and Gu, T. 2013. Study on Ultrasonic Extraction of Kerogen from Huadian Oil Shale by Solvents. *Oil Shale* **30** (4): 491-500.